JOURNAL OF GEOPHYSICAL RESEARCH, VOL. 105, NO. D13, PAGES 17,481–17,511, JULY 16, 2000

Nadir sensitivity of passive millimeter and submillimeter wave channels to clear air temperature and water vapor variations

Marian Klein

Cooperative Institute for Research in Environmental Sciences, CIRES/NOAA, University of Colorado, Boulder

Albin J. Gasiewski

National Oceanic and Atmospheric Administration, Environmental Technology Laboratory, Boulder, Colorado

Abstract. The upwelling microwave-to-submillimeter wave brightness temperature observed from above the Earth's atmosphere is sensitive to parameters such as pressure, temperature, water vapor, and hydrometeor content, and this sensitivity has been successfully used for passive vertical sounding of temperature and water vapor profiles. To determine optimal satellite observation strategies for future passive microwave instruments operating at frequencies above those now used, a study of the potential clear-air vertical sounding capabilities of all significant microwave oxygen and water vapor absorption lines in the frequency range from approximately 10 to 1000 GHz has been performed. The study is based on a second-order statistical climatological model covering four seasons, three latitudinal zones, and altitudes up to ~70 km. The climatological model was developed by comparing data from three sources: the Upper Atmosphere Research Satellite Halogen Occultation Experiment (UARS HALOE) instrument, the TIROS Operational Vertical Sounder (TOVS) Initial Guess Retrieval radiosonde set, and the NOAA advanced microwave sounder unit (AMSU) radiosonde set. The Liebe MPM87 absorption model is used for water vapor and oxygen absorption and considers the effects of ozone and isotope absorption. Variations in the vertical sounding capabilities due to statistical variations of water vapor and temperature with latitude and season around each line are considered, and useful channel sets for geostationary microwave vertical sounding are suggested.

1. Introduction

There are several motivating factors for vertical temperature and moisture sounding using microwave channels that are higher in frequency (i.e., ~200 to ~1000 GHz) than those currently employed on satellites. First, water vapor lines in this higher-frequency range are generally stronger than those below 200 GHz, thus suggesting the possibility of sensing at altitudes above the middle troposphere (Figure 1; compare section 4). The absorption spectrum over this frequency range provides a level of variation appropriate for simultaneous temperature and water vapor profiling of high-altitude regions, while the higher attenuation from the water vapor continuum in this range obscures only the lowest portion of the troposphere and only under low-to-midlatitude and summer conditions.

Second, for diffraction-limited antennas of a given size, improved spatial resolution can be obtained since the spot area decreases with the square of the frequency. The microwave channels that are commonly used for satellite water vapor and temperature vertical sounding are those around the 22.2351 and 183.3101 GHz water vapor absorption lines, e.g., as used on the Special Sensor Microwave/Imager (SSM/I), Special Sensor Microwave/Temperature and Water Vapor Profiler (SSM/T-2), and AMSU instruments, and those located within the oxygen absorption complex between ~50 and ~60 GHz, for example, as on the Microwave Sounder Unit (MSU), AMSU, and SSM/T-1. To obtain the dwell time and sampling rate necessary for the observation of severe weather, it is desirable to place microwave sensors on geostationary platforms, for example, as with the proposed NOAA Geostationary Observational and Environmental Satellite (GOES) Geosynchronous Microwave (GEM) Observatory [*Staelin et al.*, 1997]. The large geosynchronous distance demands that higher-than-mentioned microwave frequencies be used to provide good spatial resolution (~10-20 km) using diffraction-limited apertures of practical size (~2-3 m).

Third, the scattering coefficient for spherical Rayleigh ice cloud particles follows f^4a^6, where f is the frequency and a is the particle diameter [*Gasiewski*, 1993, p.#102]. One result of this sharp increase in scattering with frequency is the potential to measure cirrus cloud ice water path. It has been shown that microwave sensors operating in the wavelength range from ~1 mm to ~200 μm (i.e., ~300 GHz to ~1.5 THz in frequency) and viewing near vertically are potentially useful for direct measurements of cirrus liquid and ice water path. Proposed detection strategies include the use of both narrowband superheterodyne receivers [*Gasiewski*, 1992] and broadband Fourier transform spectrometers [*Evans et al.*, 1999]. An associated disadvantage of higher frequencies includes the

Paper number 2000JD900089.
0148-0227/00/2000JD900089$09.00

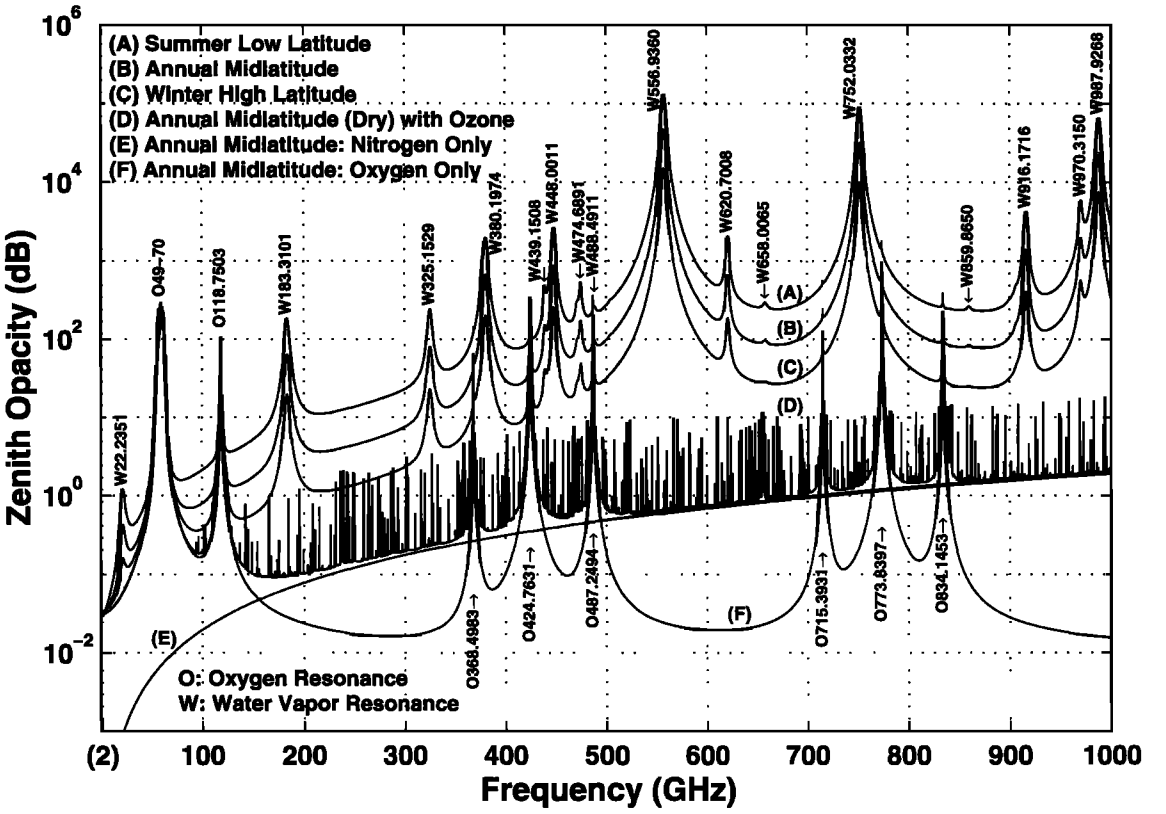

Figure 1. Total clear-air zenith opacity spectra from 2 to 1000 GHz for representative atmospheric conditions: summer low latitude, annual midlatitude, winter high latitude. Also shown are opacity spectra for dry (i.e., no water vapor) annual midlatitude conditions including ozone, nitrogen only, and oxygen only. Calculations are based on the Liebe MPM87+ absorption model (see section 4) and include only nonisotopic species. Selected strong O_2 and H_2O resonances are indicated by their center frequencies.

adverse effects of increased cloud opacity on water vapor sounding. This disadvantage can be offset, however, by using sets of water vapor sounding bands spaced approximately one to three octaves apart.

For either low-Earth orbiting (LEO) or geosynchronous (GEO) operation the selection of radiometric channels is an important design issue, the outcome of which impacts the complexity and type of the detector, the geophysical envelope of operation, and the nature of the inversion algorithms used in processing the data. The impact is large enough that precise channel selection typically occurs for most sensors in the initial phase of the design, and is exceptionally important above ~250 GHz where nascent receiver and detector technology results in higher system noise temperatures. The incremental sensitivity of radiometric channels to various atmospheric constituents, temperature and moisture in particular, is also of paramount importance in the design of retrieval algorithms for both clear and cloudy conditions. Accordingly, it is the purpose of this study to assess the vertical sounding characteristics of channels near all significant absorption lines within the frequency range of ~10-1000 GHz for satellite-based passive sensing of water vapor and temperature.

2. Incremental Weighting Functions

The incremental weighting functions (IWFs) describe the relationship between infinitesimal variations in any atmospheric parameter and the upwelling (or downwelling) brightness temperature. If $\delta p(z)$ is the variation in the profile of any atmospheric parameter p of concern, then the corresponding variation in upwelling (or downwelling) brightness temperature $T_B \overset{\Delta}{=} \lambda^2/k\, I$, where I is the radiation intensity in W m^{-2} sr^{-1} Hz^{-1}, λ is the wavelength, and k is Boltzman's constant (1.38x10^{-23} J/K), is obtained by

$$\delta T_B(f,\theta) = \int_0^\infty \delta\, p(z) W_p(z,f,\theta)\, dz\,, \tag{1}$$

where Wp is the incremental weighting function for parameter p, and θ is the observation angle measured with respect to nadir, and f is the frequency. The parameters of concern for this study are temperature T and water vapor density ρ. The IWF provides the vertical sensitivity to the observed parameter and is thus a useful tool for channel selection, sensitivity studies, inversion, and direct radiance assimilation.

The water vapor IWF derived from the nonscattering solution to the radiative transfer equation for a downward looking radiometer is [*Klein and Gasiewski*, 1998]

$$W_\rho^{\uparrow}(f,z,\theta) = \left.\frac{\partial \alpha(f,T(z),\rho(z))}{\partial \rho}\right|_{\rho^0(z)} \sec\theta\, e^{-\tau(f,z,h)\sec\theta} \left\{ \begin{array}{l} T_P(f,T(z)) - T_B^{0\downarrow RE} e^{-\tau(f,0,z)\sec\theta} - \\ \int_0^z T_P(f,T(z'))\alpha(f,T(z'),\rho(z'))\, \sec\theta\, e^{-\tau(f,z',z)\sec\theta} dz' \end{array} \right\}, \tag{2}$$
$$+ W_\rho^{\downarrow R}(f,z,\theta)$$

where

$$T_P = \frac{hf}{k\left(e^{\frac{hf}{kT}} - 1\right)} \tag{3}$$

is the Planck brightness temperature, i.e., the brightness temperature of the radiation field in local equilibrium at temperature T, and

$$W_\rho^{\downarrow R}(f,z,\theta) = e^{-\tau(f,0,h)\sec\theta} r_\beta(\theta) W_\rho^{\downarrow}(f,z,\theta) \tag{4}$$

and $W_\rho^{\downarrow}(f,z,\theta)$ is the water vapor IWF for an upward looking radiometer:

$$W_\rho^{\downarrow}(f,z,\theta) = \left.\frac{\partial\alpha(f,T(z),\rho(z))}{\partial\rho}\right|_{\rho^0(z)} \sec\theta e^{-\tau(f,h,z)\sec\theta} \left\{ \begin{array}{l} T_P(f,T(z)) - T_P(f,T_{CB}) e^{-\tau(f,h,\infty)\sec\theta} - \\ -\int_z^\infty T_P(f,T(z'))\,\alpha(f,T(z'),\rho(z'))\sec\theta e^{-\tau(f,z,z')\sec\theta} dz' \end{array} \right\} \tag{5}$$

Other terms are

$$\begin{aligned} T_B^{0\downarrow RE} &= (1 - r_\beta(\theta)) T_P(f,T_S) + r_\beta(\theta) T_B(f,0,\infty) \\ T_B(f,0,\infty) &= \int_0^\infty T_P(f,T(z))\,\alpha(f,T(z),\rho(z))\ \sec\theta e^{-\tau(f,0,z)\sec\theta} dz \\ &\quad + T_P(f,T_{CB}) e^{-\tau(f,0,\infty)\sec\theta} \end{aligned} \tag{6}$$

and $\tau(f,z_1,z_2) = \int_{z_1}^{z_2} \alpha(f,T(z'),\rho(z'))\,dz'$ is the opacity between levels z_1 and z_2. The units of equations (2) and (5) are in, for example, K km^{-1} g^{-1} m^3.

The temperature IWF for a downward looking radiometer can be similarly calculated:

$$W_I^{\uparrow}(f,z,\theta) = \sec\theta e^{-\tau(f,z,h)\sec\theta} \left\{ \begin{array}{l} \left.\frac{\partial T_P}{\partial T}\right|_{I^0(z)} \alpha(f,T(z),\rho(z)) + \left.\frac{\partial\alpha(f,T(z),\rho(z))}{\partial T}\right|_{I^0(z)} \\ \left[\begin{array}{l} -\int_0^z T_P(f,T(z'))\,\alpha(f,T(z'),\rho(z'))\sec\theta e^{-\tau(f,z,z')\sec\theta} dz' - \\ T_P(f,T(z)) - e^{-\tau(f,0,z)\sec\theta} \cdot \\ \left\{ (1 - r_\beta(\theta)) T_P(f,T_S) + r_\beta(\theta) \left[T_B(f,0,\infty) + W_T^{\downarrow}(f,z,\theta) \right] \right\} \end{array} \right] \end{array} \right\} \tag{7}$$

where $W_T^{\downarrow}(f,z,\theta)$ is the temperature IWF for an upward-looking radiometer:

$$W_T^{\downarrow}(f,z,\theta) = \sec\theta e^{-\tau(f,h,z)\sec\theta} \left\{ \begin{array}{l} \left.\frac{\partial T_P}{\partial T}\right|_{I^0(z)} \alpha(f,T(z),\rho(z)) + \left.\frac{\partial\alpha(f,T(z),\rho(z))}{\partial T}\right|_{I^0(z)} \\ \left[\begin{array}{l} -T_P(f,T(z)) - T_P(f,T_{CB})\, e^{-\tau(f,z,\infty)\sec\theta} - \\ -\int_z^\infty T_P(f,T(z'))\,\alpha(f,T(z'),\rho(z'))\sec\theta e^{-\tau(f,z,z')\sec\theta} dz' \end{array} \right] \end{array} \right\} \tag{8}$$

The units of equations (7) and (8) are, for example, in km^{-1}. The terms in the above equations and other preferred units are

α = total absorption coefficient (Np/km);
$T(z)$ = physical temperature at atmospheric height z (K);
$\rho(z)$ = water vapor density (kg m^{-3});
h = observation height (m);
r_β = surface reflection coefficient for polarization β;
T_S = surface temperature (K);
T_{CB} = cosmic background temperature (K)

and the term $\partial T_P/\partial T$ is the first derivative of the Planck brightness temperature (equation (3)). The temperature IWF is least variable (and thus useful for temperature sounding) around absorption lines of well-mixed species of constant density. By far the most practical microwave lines for temperature sounding are those of O_2.

Numerical quadrature over nonuniformly spaced height levels is used in the evaluation of the IWF. Terms such as

$$\int_z^\infty T_P(f,T(z'))\,\alpha(f,T(z'),\rho(z'))\sec\theta e^{-\tau(f,z,z')\sec\theta} dz' \tag{9}$$

are calculated by casting the solution into an integral over the transmissivity t:

$$\begin{aligned} &\int_z^\infty T_P(f,T(z'))\,\alpha(f,T(z'),\rho(z'))\sec\theta e^{-\tau(f,z,z')\sec\theta} dz', \\ &= \int_0^1 T(t)\,dt \end{aligned} \tag{10}$$

where t and the opacity $\tau(f,z1,z2)$ are

$$t = e^{-\tau(f,z_1,z_2)} \tag{11}$$

$$\tau(f,z_1,z_2) = \int_{z_1}^{z_2} \alpha(f,T(z),\rho(z))\sec\theta dz\,. \tag{12}$$

The incremental transmissivity dt is evaluated as (detailed description of the quadrature method can be found in the work of Gasiewski [1993, chap. 3.3.2])

$$dt = \alpha(f,T(z),\rho(z))\sec\theta e^{-\int_{z_1}^{z} \alpha(f,T(z'),\rho(z'))\sec\theta dz'} dz\,. \tag{13}$$

The Planck brightness temperature is evaluated for each atmospheric level as well as for the cosmic background and surface. In this study the surface temperature is assumed to be fixed and independent of the temperature of the bottom layer of the atmosphere. The above IWFs can be used to form the elements of the Jacobian for clear-air direct radiance data assimilation [*Phalippou*, 1996].

3. Climatological Statistics

Calculations of the water vapor IWF reveal rather enormous absolute sensitivities (of the order of ~10^6 K km^{-1} g^{-1} m^3) for upper stratospheric and mesospheric levels near the center of many water vapor lines (e.g., Figure 2, for the 183.3101 GHz line). The total density of water vapor, however, is typically between 2 and 3 ppmv (parts per million by volume) at these levels. Thus changes of significance (e.g. > ~ 10^{-6} gm^{-3} over more than 1 km) are improbable, and the typical brightness response to natural water vapor variations at these altitudes is both moderate and linear. To analyze the natural response, it is necessary to first characterize the mean vapor density of the atmosphere as well as the covariance of water vapor variations.

Atmospheric water vapor statistics vary considerably with season, location, and altitude in both mean and covariance.

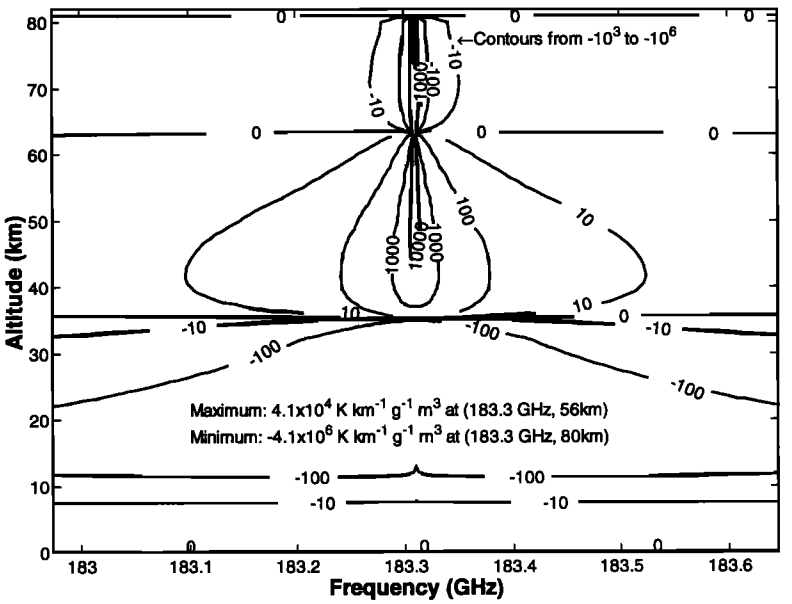

Figure 2. Water vapor IWF contours near 183 GHz in units of (K km^{-1} g^{-1} m^3) for 300 km observation height, ocean background, and nadir view. The calculations use the 1976 U.S. Standard Atmosphere augmented with water vapor up to 80 km altitude and 80% surface relative humidity.

Accordingly, we have developed a second-order statistical model for temperature and humidity covering altitudes up to ~70 km and applicable for a variety of latitudes and seasons. Three sources of data were used to develop this model: (1) the Halogen Occultation Experiment (HALOE) instrument onboard the Upper Atmosphere Research Satellite (UARS) [*Russel et al.*, 1993], (2) the TIROS Operational Vertical Sounder (TOVS) Initial Guess Retrieval (TIGR) set [*Chedin et al.*, 1985] based on radiosonde and rocketsonde measurements, and (3) the NOAA AMSU radiosonde test set.

3.1. HALOE Observations

The HALOE instrument on the UARS was launched on September 12, 1991, and began scientific observations in October 1991. The instrument uses solar occultation of selected portions of the spectral range from 2.45 to 10.04 μm via limb absorption to obtain vertical profiles of O_3, HCl, HF, CH_4, H_2O, NO, NO_2, aerosol extinction, and temperature. A detailed description of the HALOE measurement technique can be found in the work of *Russel et al.* [1993].

A limb path contains 30 to 60 times more absorber compared to a nadir sounding path and thus provides higher sensitivity to water vapor at extremely low concentrations. On the other hand, the lower in altitude a limb path passes into the atmosphere, the larger the number of altitude levels are convoluted into the final measurement. The retrieval technique is robust enough and the instantaneous field of view is narrow enough, however, to provide vertical resolution better than ~2 km over the altitude range from a few kilometers to the ~75 km. The HALOE instrument is virtually self-calibrating because each vertical profile of gas mixing ratio is determined by computing the ratio of the solar energy attenuated by the atmospheric limb to the nonattenuated background measurements obtained via paths passing outside of the atmosphere. A disadvantage of the HALOE technique is that measurements can be performed only at local sunrise and sunset times, thus limiting sampling to 15 sunrises and 15 sunsets each day. Geographic coverage is also constrained in that the satellite covers only latitudes lower than 80°. In addition, occultation cannot be performed during polar winters due to the need of a solar background view. Nevertheless, the HALOE sensor has operated for over 6 years and the retrieved profile database contains a large number of independent parameters.

The second-order HALOE statistics for this study were developed using data from October 1991 to September 1997. First, for each of the 271 pressure levels, 4 seasons, and 3 latitude zones, the total standard deviations σ_R^2 of the reported water vapor mixing ratio and temperature were calculated. The total standard deviation is the sum square of the standard deviation of the retrieval noise (including instrument noise) σ_I^2 and the standard deviation of the geophysical parameter of concern σ_P^2, namely,

$$\sigma_R^2 = \sigma_I^2 + \sigma_P^2, \tag{14}$$

where $p = T$ for temperature or ρ for humidity. For each retrieved parameter in the HALOE database an estimate of the standard deviation of the retrieval noise σ_I^2 was provided. To limit the propagation of instrument noise, only the measurements that complied with the condition

$$\sigma_I^2 \le \frac{\sigma_R^2}{2} \tag{15}$$

were considered as valid samples. In other words, the signal-to-noise ratios (SNRs) for samples used in developing the statistics are better than 0 dB. After such an evaluation it was concluded that HALOE measurements satisfy the above condition for temperature measurements between ~35 and ~75 km altitude and for water vapor measurements from ~12 to ~35 km altitude. The number of valid samples found

Table 1. Number of HALOE Temperature/Water Vapor Profiles Used in the Second Order Climatological Study

Latitude / Season	High (60°-90°)	Middle (30°-60°)	Low (0°-30°)
Spring	5350/3815	4987/3424	3416/2127
Summer	4775/3602	3105/1966	2200/1575
Fall	1544/948	8585/6295	3615/2367
Winter	0/0	8733/5698	3380/2366

through this procedure for HALOE temperature and water vapor profiles are summarized in Table 1.

The HALOE data were next sorted into appropriate bins according to their latitude and season, and then grouped according to pressure. For all pressure levels the standard deviation σ_P^2 was evaluated and all measurements that did not satisfy condition (15) were rejected. Only profiles that were valid for all selected pressure levels were used in statistical calculation.

3.2. TIGR Profile Set

The TIGR database was described by *Chedin et al.* [1985] and since improved as described by *Cheury et al.*, [1995] and *Francois and Ottle* [1996]. The TIGR set groups 1 761 representative atmospheric samplings selected from 85,000 radiosonde and rocketsonde reports collected around the globe during all seasons for the period from 1976 to 1989. Data are available at 40 pressure levels from the surface to 0.05 mbar (~70 km altitude) for temperature, water vapor, and ozone mixing ratio. The primary sources of radiosonde data are files regularly archived by NOAA National Environmental Satellite, Data and Information Service (NESDIS) and the radiosonde archive of the French Meteorological Office. Although the TIGR database contains a smaller number of samples than the HALOE database, it is based on direct (rather than inferred) measurements and covers the entire vertical range from the surface to the mesosphere. The number of sample profiles in each of the defined latitudinal/seasonal bins ranged between 20 and 423, providing a reasonably large ensemble for statistical purposes.

3.3. NOAA AMSU Radiosondes

The NOAA AMSU test database is an ensemble of 715 atmospheric profiles based on radiosonde and rocketsonde reports from several sites around the globe. This data set was first used in the early 1980s for temperature retrieval studies using the then-proposed AMSU system. The AMSU radiosondes provide temperature measurements from the surface to ~0.1 mbar pressure (~65 km altitude) and water vapor measurements from the surface to ~15 km altitude. The number of sample profiles for each latitudinal/seasonal bin ranged between 26 and 90 and, again, provided a reasonably large ensemble.

3.4. Climatological Model Intercomparison

Prior to adoption of a specific second-order climatological model the covariance and correlation matrices were evaluated for all three databases for temperature and water vapor over all valid latitude ranges. In general, from winter high latitude to summer low latitude the mean tropospheric temperature from the databases increased from 30° to 40°C, the mean tropopause temperature decreased ~15°C, the mean mesospheric temperature increased ~13°C, and temperature standard deviations increased by a factor of ~2. For water vapor the mean density increased by a factor of ~20 from winter high latitude to summer low latitude, and the density standard deviation increased by approximately 1 order of magnitude. The wide range of variation of these statistics warrants the use of climatological models in computing IWFs, in particular, for water vapor.

Good overall agreement in all latitudinal and seasonal bins was found among the three sets for both means and standard deviations (e.g., Figure 3) for those overlapping altitude ranges and the available seasonal/latitudinal bins. Although a general statistical consistency was found among these sets, the TIGR database was adopted for further studies because of its (1) full global coverage and (2) water vapor profile information over the full altitude range from the surface to ~70 km.

4. Absorption by Atmospheric Gases

The accuracy of any IWF calculation is contingent on that of the underlying absorption model. Prior to IWF calculations the line parameters and brightness temperatures, computed using two absorption models for nonisotopic oxygen, water vapor, and nitrogen, were compared for consistency. These models were (1) the MPM87 absorption model of *Liebe* [1983, 1987] as modified by the addition of six nonoverlapping submillimeter wave oxygen lines [*Gasiewski*, 1992] and an additional N_2 absorption model [*Birnbaum et al.*, 1982] (hereinafter refered to as MPM87+), and (2) the absorption model of *Rosenkranz* [1993], as modified by Rosenkranz by the addition of eight weak water vapor lines at 321.2256, 439.1508, 443.0183, 470.8890, 474.6891, 488.4911, 620.7008, and 916.1712 GHz.

4.1. Water Vapor, Oxygen, and Nitrogen Model Intercomparisons

The 41 O_2 lines used in the two models are identical except for small corrections to the MPM87 broadening and overlap coefficients by Rosenkranz; these corrections were made based upon additional O_2 absorption measurements by *Liebe et al.* [1991] and published in a revised 1993 version of MPM87 (MPM93, *Liebe et al.* [1993]). Otherwise, the Rosenkranz model uses fewer water vapor lines than MPM87+ (about one half as many; see Table 2) and is reportedly valid for frequencies up to ~800 GHz. MPM87+ includes some weak H_2O lines that belong to the ν_2 vibrational state. Both include nearly identical collision-induced nitrogen absorption models, the major difference being that the exponent on the inverse temperature factor $(300/T)$ is 4.50 for the MPM87+ N_2 model and 3.55 for the Rosenkranz N_2 model. Nadir brightness temperature calculations over extremely cold dry oceanic (i.e., worst-case difference) conditions using the two N_2 models agree, however, to within 0.7 K. Thus the N_2 components of the MPM87+ and Rosenkranz models are effectively equivalent for this study (It is noted that the N_2 absorption model published by Rosenkranz in the work of *Janssen* [1993] is significantly more absorbing (by up to ~65% below 1000 GHz) than either of the current Rosenkranz or MPM87+ N_2 models. The 1993 model was based on work by *Dagg et al.*

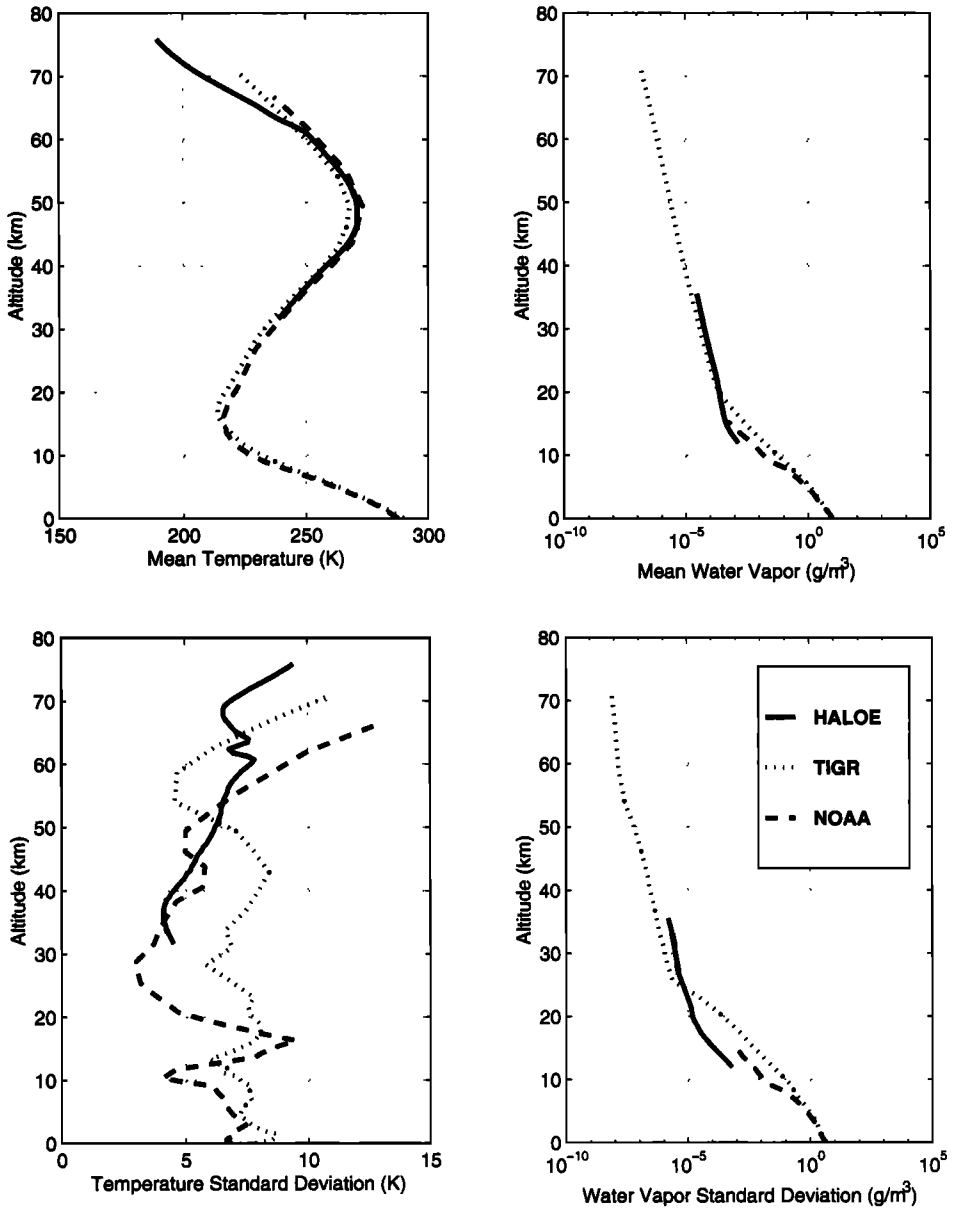

Figure 3. Comparison of the temperature and water vapor density profiles and their standard deviations, from HALOE, TIGR, and NOAA climatologies for the summer and middle-latitude case.

[1975, 1978], and accounts for up to a ~2 K difference in nadir brightness compared to MPM87+). In neither of the absorption models for this study was Zeeman splitting accommodated; thus the validity of the results is restricted up to ~40 km altitude, or within ~2.5 MHz of oxygen absorption line centers.

Both the Rosenkranz and the MPM87+ attenuation models for H_2O and O_2 (Table 3) were checked against the current Jet Propulsion Laboratory (JPL) online microwave spectral line catalog [*Poynter and Pickett*, 1985]. From Table 2, all ν_1 water vapor lines, listed in the JPL catalog, which are of significant strength for the vapor and total pressures encountered in the terrestrial atmosphere are included in MPM87+, and the strongest of those are included in the Rosenkranz model. Twenty-six weak oxygen lines near the 5-mm O_2 band which are listed in the JPL online catalog are not used in either the MPM87+ or the Rosenkranz model since they are insignificant for nadir sounding in the terrestrial atmosphere.

In addition to small differences in line parameters, the MPM87+ and Rosenkranz models also differ in their water vapor continuum terms. In a recent reanalysis by *Rosenkranz* [1998] of the available data on H_2O continuum absorption it was concluded that the continuum model in MPM87 more accurately represents foreign broadening, while a revised continuum model defined in MPM93 better represents self broadening. In the Rosenkranz model the continuum term is accordingly based on an appropriate combination of these models (indicated by MPMf87/s93 in the work of *Rosenkranz*, [1998]). Since foreign broadening is dominant in the terrestrial atmosphere, it is concluded that either the Rosenkranz or the MPM87+ continuum models are applicable

Table 2. Comparison of Water Vapor Absorption Lines for Various Microwave Models

Frequency JPL Catalog (GHz)	Line Strength JPL Catalog (cm^2 Hz)	Frequency Rosenkranz (GHz)	Frequency MPM87+ (GHz)
22.235	1.3146e-014	22.2351	22.23508
67.80396	4.1267e-16		67.81396 (ν_2)
119.99594	4.7720e-016		119.99594 (ν_2)
183.31	2.2751e-012	183.3101	183.310117
321.23	8.0742e-014	321.2256	321.225644
325.15	2.6996e-012	325.1529	325.152919
336.2226008	1.8080e-015		336.187000 (ν_2)
380.2	2.4423e-011	380.1974	380.197372
390.13	9.2619e-015		390.134508
437.35	1.5024e-013		437.346667
439.15	2.1812e-012	439.1508	439.150812
443.02	4.6249e-013	443.0183	443.018295
448	2.5651e-011	448.0011	448.001075
470.89	8.3657e-013	470.8890	470.888947
474.69	3.2802e-012	474.6891	474.689127
488.49	6.6988e-013	488.4911	488.491133
503.57	1.0132e-013		503.568532
504.48	3.39e-014		504.482692
556.94	1.5321e-009	556.9360	556.936002
620.7	1.708e-011	620.7008	620.700807
645.73	7.7321e-015		
645.87	2.3206e-014		
658.0052803	1.0120e-012		658.006500 (ν_2)
752.03	1.0137e-009	752.0332	752.033227
766.8	5.4613e-015		
841.05	5.9676e-014		841.073593
859.9623128	6.4269e-013		859.865000 (ν_2)
862.72	4.7841e-015		
862.74	1.5948e-015		
899.3066749	2.7657e-013		899.407000 (ν_2)
902.6161733	1.9418e-013		902.555000 (ν_2)
906.21	8.9764e-013		906.205524
916.17	4.2394e-011	916.1712	916.171582
970.32	4.7984e-011		970.315022
987.93	7.357e-010		987.926764

for this study. In any case, the differences in brightness temperature produced between these continuum models for the range of temperature, pressure, and vapor values encountered within the terrestrial atmosphere are insignificant compared to typical radiometer accuracies.

The brightness difference spectrum ($T_{\text{Rosenkranz}}$-$T_{\text{MPM87+}}$) within the range from 1-800 GHz over an ocean background for two extreme atmospheric profiles is shown in Figure 4. The calculations are based on the quadrature algorithm described by *Gasiewski and Staelin* [1990] as implemented in the program Microwave Radiative Transfer (MRT), version 6.12. The difference spectrum can be considered to be the result of absorption model differences either near absorption lines or within window regions. The near-line differences are primarily the result of small differences in line strength and broadening parameters, while the window region differences are the result of different parameters for the water vapor continuum and nitrogen models. To better understand the difference spectrum, consider the attenuation for a specific constituent (e.g., O_2, H_2O) evaluated at a level of one optical depth for the two extreme atmospheric cases (Figures 5 and 6 for H_2O and O_2, respectively). The peaks of the IWFs for temperature and (for regions of approximately constant vertical lapse rate) water vapor occur near one optical depth; a

Table 3. Comparison of Oxygen Absorption Lines for Various Microwave Models

Frequency JPL Catalog (GHz)	Line Strength JPL Catalog (cm^2 Hz)	Frequency Rosenkranz (GHz)	Frequency MPM87+ (GHz)
44.9070918	8.4528e-025		
45.4091561	4.0402e-024		
45.911794	1.8315e-023		
46.4150628	7.8723e-023		
46.9190273	3.207e-022		
47.4237611	1.2379e-021		
47.9293489	4.5258e-021		
48.4358887	1.5668e-020		
48.9434953	5.1333e-020		
49.4523037	1.5918e-019		
49.9624752	4.6677e-019		
50.4742042	1.2939e-018		
50.9877278	3.3892e-018		
51.5033389	8.3869e-018	51.5034	51.5034
52.0214047	1.9593e-017	52.0214	52.0214
52.5423925	4.3172e-017	52.5424	52.5424
53.0669079	8.9702e-017	53.0669	53.0669
53.5957507	1.7559e-016	53.5957	53.5957
54.1300016	3.2352e-016	54.1300	54.1300
54.671145	5.6027e-016	54.6712	54.6712
55.221372	9.1075e-016	55.2214	55.2214
55.783819	1.3874e-015	55.7838	55.7838
56.264766	8.0408e-016	56.2648	56.2648
56.363393	1.9747e-015	56.3634	56.3634
56.96818	2.617e-015	56.9682	56.9682
57.6124802	3.2129e-015	57.6125	57.6125
58.323885	3.6241e-015	58.3239	58.3239
58.44658	2.2167e-015	58.4466	58.4466
59.164215	3.7042e-015	59.1642	59 1642
59.590978	3 2772e-015	59.5910	59.5910
60.306044	3.3366e-015	60.3061	60.3061
60.434776	3 8735e-015	60.4348	60.4348
61.15057	3.9893e-015	61.1506	61.1506
61.800155	3.7e-015	61.8002	61.8002
62.411223	3.1434e-015	62.4112	62.4112
62.486255	2.4706e-015	62.4863	62.4863
62.9979772	2.4683e-015	62.9980	62.9980
63.56852	1.803e-015	63.5685	63.5685
64.127777	1.2294e-015	64.1278	64.1278
64.6788985	7.8487e-016	64.6789	64.6789
65.2240647	4.7011e-016	65.2241	65.2241
65.764744	2.6467e-016	65.7648	65.7648
66.3020821	1.4018e-016	66.3021	66.3021
66.8368204	6.9952e-017	66.8368	66.8368
67.3695887	3.29e-017	67.3696	67.3696
67.900867	1.4598e-017	67.9009	67.9009
68.431005	6.1136e-018		
68.960312	2.4188e-018		
69.48903	9.0427e-019		
70.0173699	3.196e-019		
70.5454815	1.0683e-019		
71.0735108	3.3799e-020		
71.6015781	1.012e-020		
72.1297874	2.8695e-021		
72.6582294	7 7055e-022		
73.1869841	1.9611e-022		
73.716123	4.7315e-023		
74.2457103	1.0827e-023		
74.775804	2.3496e-024		
118.750343	2.9431e-015	118.7503	118.7503
368.4983443	6.4313e-016	368.4984	368.4983
424.76312	7.117e-015	424.7631	424.7631
487.2493755	3.0896e-015	487.2494	487.2494
715.393072	1.7956e-015	715.3932	715.3931
773.839691	1.1639e-014	773.8397	773.8397
834.1457191	4.1267e-015	834.1453	834.1453

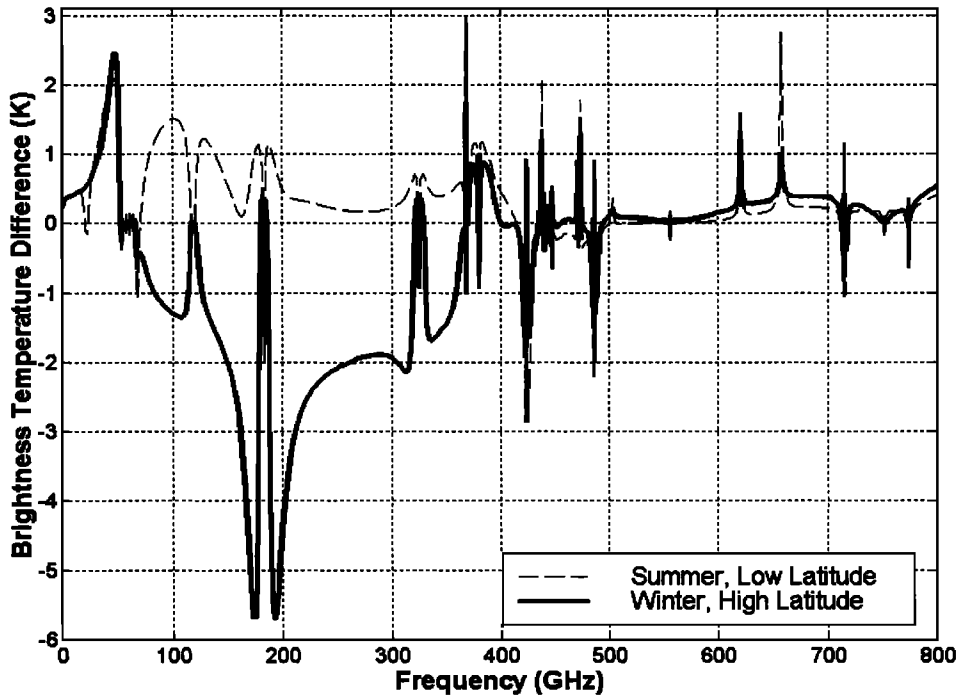

Figure 4. Brightness temperature difference between Rosenkranz and MPM87+ absorption models evaluated for nadir satellite view for two extreme atmospheric cases and ocean background.

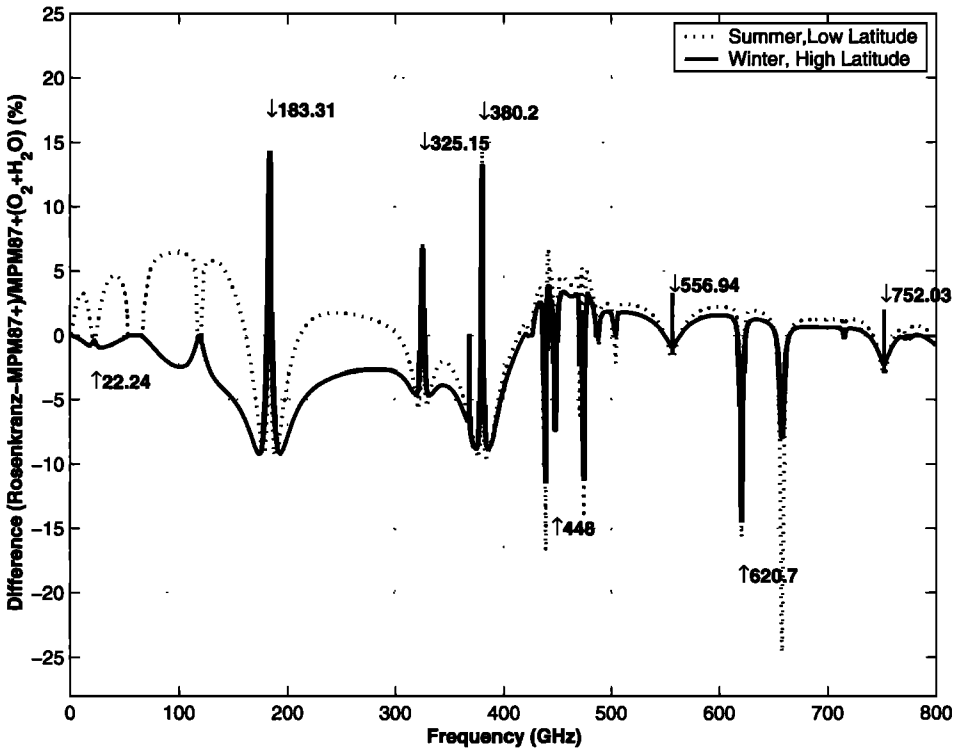

Figure 5. Relative difference spectra of calculated attenuation between Rosenkranz and MPM87+ absorption models for water vapor evaluated for two extreme atmospheric states at the level of one optical depth. Arrows point to the center of the absorption lines.

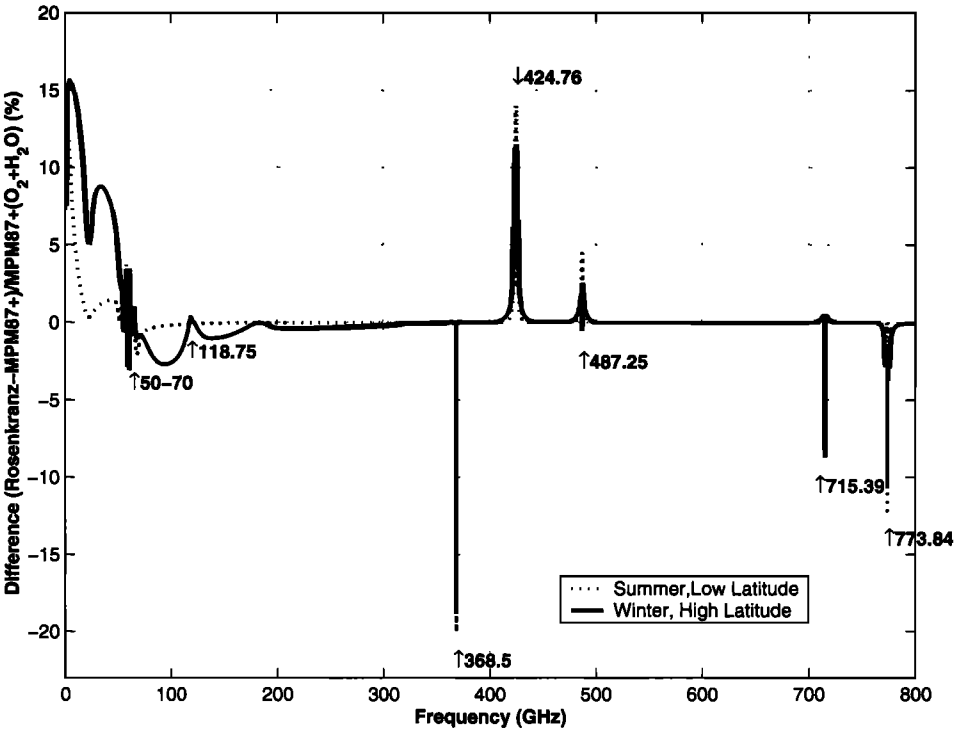

Figure 6. Relative difference spectra of calculated attenuation between Rosenkranz and MPM87+ absorption models for oxygen evaluated for two extreme atmospheric states at the level of one optical depth. Arrows point to the center of the absorption lines.

small attenuation difference will thus shift the altitude of maximum IWF sensitivity. We define a relative difference in opacity R_D (in percent) by

$$R_D = \frac{\tau_{ROS} - \tau_{MPM87+}}{\tau_{MPM87+\_TOT}} \times 100, \quad (16)$$

where τ_{ROS} and τ_{MPM87+} are the attenuations for given constituents calculated using the Rosenkranz and MPM87+ absorption models, respectively, and τ_{MPM87+_TOT} is the total attenuation (H_2O, O_2, and N_2) evaluated using the MPM87+ absorption model.

Although nonresonant nitrogen differences can account for discrepancies of as much as ~0.5 K in oceanic nadir brightness temperature below ~400 GHz, water vapor continuum differences dominate in this region and account for as much as ~7% discrepancy in opacity (Figure 5). Since water vapor opacity is manifested over a path of ~3-5 km length, the associated difference in the peak altitude of the temperature weighting function is ~200-350 m. Assuming a lapse rate of ~7 K/km, such height discrepancies are seen to be consistent with the window region brightness differences of Figure 4 (~2-3 K). The maximum brightness discrepancy of ~ -5.7 K (i.e., ~800 m height discrepancy) occurs at ~190 GHz and is the result of small differences in the line strength and broadening parameters of the 183.310 GHz H_2O line. Such differences in the H_2O line-broadening parameters account for differences in relative absorption of up to 25% (Figure 5). Figure 6 shows that except for frequencies below ~50 GHz, oxygen absorption differs by ~5-20% (i.e., ~250-1000 m in height difference) but only near the absorption line centers and for frequencies above ~368 GHz. Above ~400 GHz the nonresonant nitrogen models contribute to discrepancies of as much as ~0.4 K in window regions.

While comparisons with measured data can, in principal, be used to determine which absorption model is more precise, instrumental uncertainties caused by radiometer calibration errors or atmospheric profile measurement errors are usually comparable to the differences produced by the herein-examined models. Indeed, currently available radiometer data are not accurate enough to empirically discriminate between these models at frequencies from ~100 GHz to ~10 THz. Nonetheless, if we consider the absorption model differences described above to be characteristic of the current knowledge of atmospheric absorption theory, then it can be assumed that the IWF height calculations in this study are accurate to ~1 km altitude for the worst-case scenario and typically to within a few hundred meters. In comparison, such height uncertainties in water vapor IWFs are comparable to or only slightly greater than those height uncertainties expected from imperfect knowledge of the temperature profile alone; that is, a 1-2 K temperature profile error will shift the peak altitude of temperature-weighting functions for water vapor by a similar vertical distance of ~100-200 m. Accordingly, both models are reasonably consistent for these IWF studies and further calculations presented herein used the MPM87+ absorption model in MRTv6.12.

4.2. Ozone and Isotopic Species

In addition to those of O_2, H_2O, and N_2 the effects of stratospheric ozone on nadir sounding were considered by augmenting MPM87+ with a non isotopic O_3 absorption model incorporating the JPL set of 1583 O_3 lines from 10 to

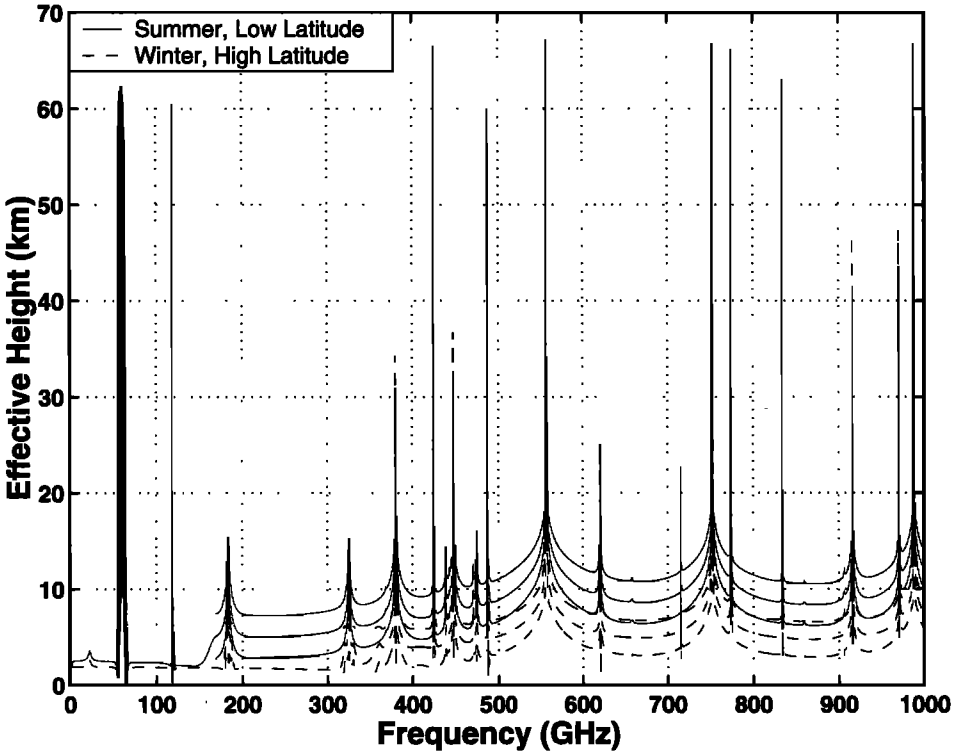

Figure 7. Effective water vapor sensing height $h_{\text{eff},\rho}$ along with $h_{\text{eff},\rho} \pm \sigma_{h,\rho}$ for two extreme atmospheric profiles, satellite nadir view over ocean background. Ozone influence is not considered.

1300 GHz. All O_3 line strength and state energy parameters were obtained from the JPL database, while broadening parameters were obtained from the listing of *Rosenkranz* [1993]. The ozone model was used in IWF calculations to indicate those spectral regions wherein special filtering or interpretation requirements are warranted. With only a few exceptions (as discussed in section 6), the effects of O_3 absorption over the relatively wide bandwidths useful for nadir sounding can be safely neglected for sounding purposes.

While the isotopic water vapor species H_2O^{17}, H_2O^{18}, and HDO exhibit strong absorption lines, their low natural abundances make these species less significant than nonisotopic H_2O for nadir sounding purposes. When scaled by their natural abundances, it is found that only six of the strongest isotopic lines (at 323.8265 and 385.7865 GHz for H_2O^{17} and 322.4652, 390.6078, 489.0543, and 520.1373 GHz for H_2O^{18}) are comparable in strength to any nearby weak lines in the MPM87+ model. We limit our discussion here by simply noting the existence of these isotopic lines and focusing mostly on the much stronger nonisotopic lines.

5. Incremental Weighting Function Statistics

Nadir IWFs for temperature and water vapor were evaluated on the above nonuniform frequency grid from 10 to 1000 GHz assuming an ocean background [*Wilheit*, 1979], an observation height of 150 km, and clear air conditions. In all calculations the values of ocean surface temperature were based on the climatology of *Isemer et al.* [1985] and vary from 275 K for high latitudes to 301 K for low latitudes; the wind speed was selected to be 7 m/s (near the mean value of wind speed over oceans). While IWFs over land would also be of interest, the geographical predominance of the oceans, their importance in the generation of severe and damaging weather, the relative lack of meteorological data over them, and their relative simplicity of electromagnetic characterization warrant their exclusive use for this study. We note, however, that for frequencies above ~200 GHz, near-line centers, or frequencies above ~80 GHz for moist conditions the high zenith opacity of the atmosphere renders inconsequential the choice of surface model. We have also specifically excluded the absorption and scattering effects of hydrometeors from this study in order to focus on the clear-air problem; the characteristics of IWFs in the presence of hydrometeors are currently under study and will be the focus of a future publication.

Figures 7, 12a, and 13a show the effective water vapor sounding heights $h_{\text{eff},\rho}$ for two extreme climatological cases along with the IWF widths $\sigma_{h,\rho}$ defined by

$$h_{\text{eff},\rho} = \frac{\int_0^\infty z \left| W_\rho(f,z,\theta)\,\sigma_\rho \right| dz}{\int_0^\infty \left| W_\rho(f,z,\theta)\,\sigma_\rho \right| dz}, \tag{17}$$

$$\sigma_{h,\rho} = \sqrt{\frac{\int_0^\infty (z - h_{\text{eff}})^2 \left| W_\rho(f,z,\theta)\,\sigma_\rho \right| dz}{\int_0^\infty \left| W_\rho(f,z,\theta)\,\sigma_\rho \right| dz}}. \tag{18}$$

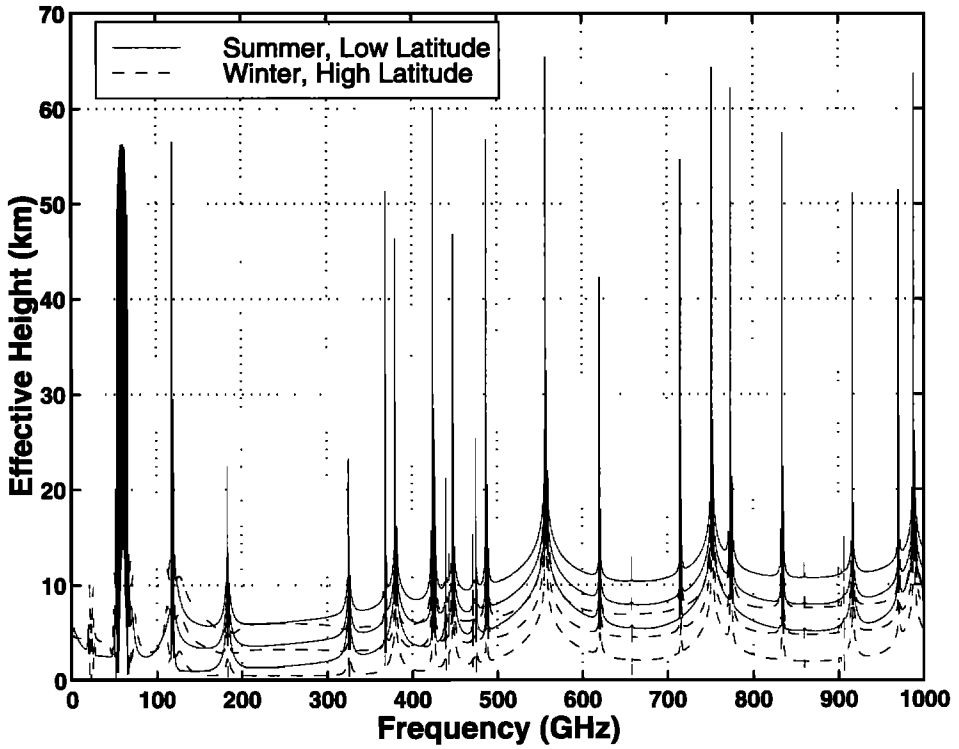

Figure 8. Effective temperature sensing height $h_{\mathrm{eff},T}$ along with $h_{\mathrm{eff},T} \pm \sigma_{h,T}$ for two extreme atmospheric profiles, satellite nadir view over ocean background. Ozone influence is not considered.

In equations (17) and (18) the water vapor IWFs $W\rho$ were multiplied by the standard deviation profile of water vapor (σ_ρ) for the respective season and latitudinal zone. The effective temperature-sounding heights $h_{\mathrm{eff},T}$, together with the width $\sigma_{h,T}$ for the same extreme atmospheric situations, are similarly shown in Figures 8, 14a, and 15a and were evaluated as follows:

$$h_{\mathrm{eff},T} = \frac{\int_0^\infty z\left|W_T(f,z,\theta)\right|dz}{\int_0^\infty \left|W_T(f,z,\theta)\right|dz}, \tag{19}$$

$$\sigma_{h,T} = \sqrt{\frac{\int_0^\infty (z-h_{\mathrm{eff}})^2\left|W_T(f,z,\theta)\right|dz}{\int_0^\infty \left|W_T(f,z,\theta)\right|dz}}. \tag{20}$$

Figures 9 and 10 show the corresponding upwelling brightness temperature variations $\sigma_{TB,p}$ due to the natural variation of water vapor content and temperature in the clear atmosphere.

$$\sigma_{TB,p} = \sqrt{\overline{W}_p^t \overline{\overline{R}}_{pp} \overline{W}_p}, \tag{21}$$

where $\overline{W}_p$ is the incremental (column) weighting vector (e.g., in units of K g^{-1} m^{-3} for water vapor and dimensionless for temperature), and $\overline{\overline{R}}_{pp}$ is the covariance matrix for parameter p, where p is either water vapor content or temperature. The variation σ_{TB} can be interpreted as the minimum sensitivity that the radiometer measuring the parameter of interest must possess to be able to sense natural atmospheric variations in that parameter. Figures 12b-15b also show plots of brightness temperature variations indexed by sounding height rather than by frequency. Plots are printed separately for each significant absorption line in the frequency range of concern, with the appropriate absorption line frequency given above each plot. Both upper and lower wings of each absorption line are shown.

An unexpected feature can be seen in the effective sounding height spectrum, for example, Figure 13 (a2) and (a3), Figure 15 (a1), for the 183.3101 and 325.1529 GHz water vapor absorption lines, and for the 118.7503 GHz oxygen absorption line. The effective sounding height monotonically decreases with increasing frequency offset from the line center (e.g., out to ~2 GHz for the 183.3101 GHz line; see Figure13 (a2)) and then exhibits an inflection, increasing abruptly with further offset. A (second) negative inflection occurs at a larger offset. These inflections occur at frequencies where the predominant source of the upwelling radiance changes from direct emission from the atmosphere (for the first inflection) or cold reflection from the surface (for the second inflection) to a mixture of direct and reflected emission. The transitions cause a change in the sign of the IWF for low altitudes (first inflection; see Figure 11) or midtropospheric altitudes (second inflection), the result of which is a subtle increase (then decrease) in the sounding height as defined by either equations (17) or (19). Such inflections are the result of high surface reflectivity and are not present over land.

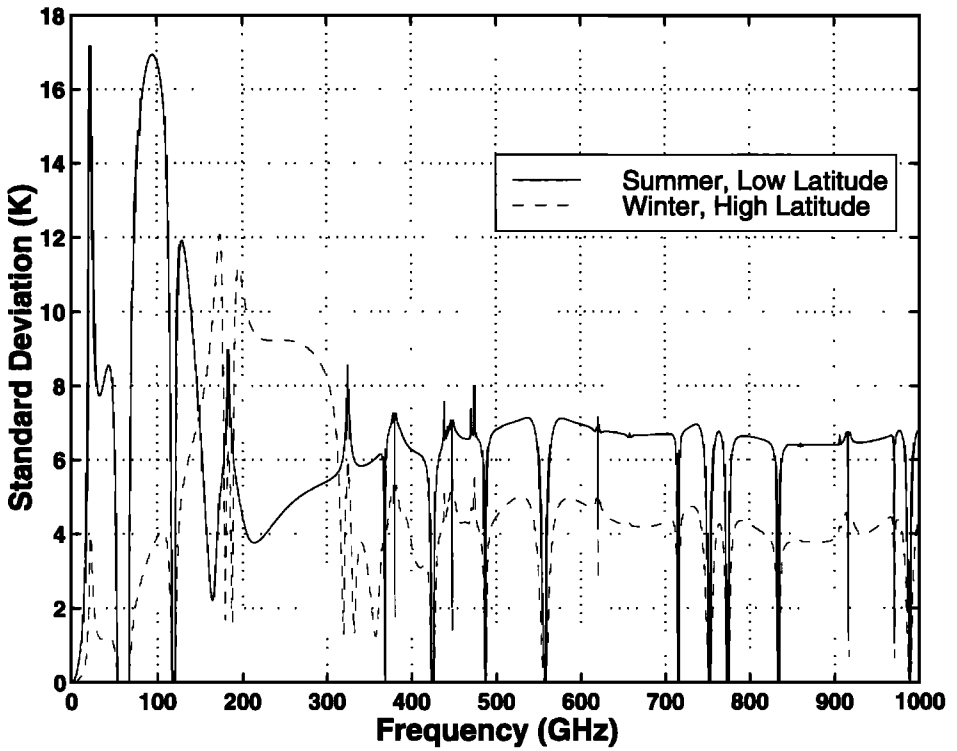

Figure 9. Standard deviation $\sigma_{h,\rho}$ of upwelling brightness temperature due to the variations in water vapor content for two extreme atmospheric profiles, nadir view over ocean background. Ozone influence is not considered.

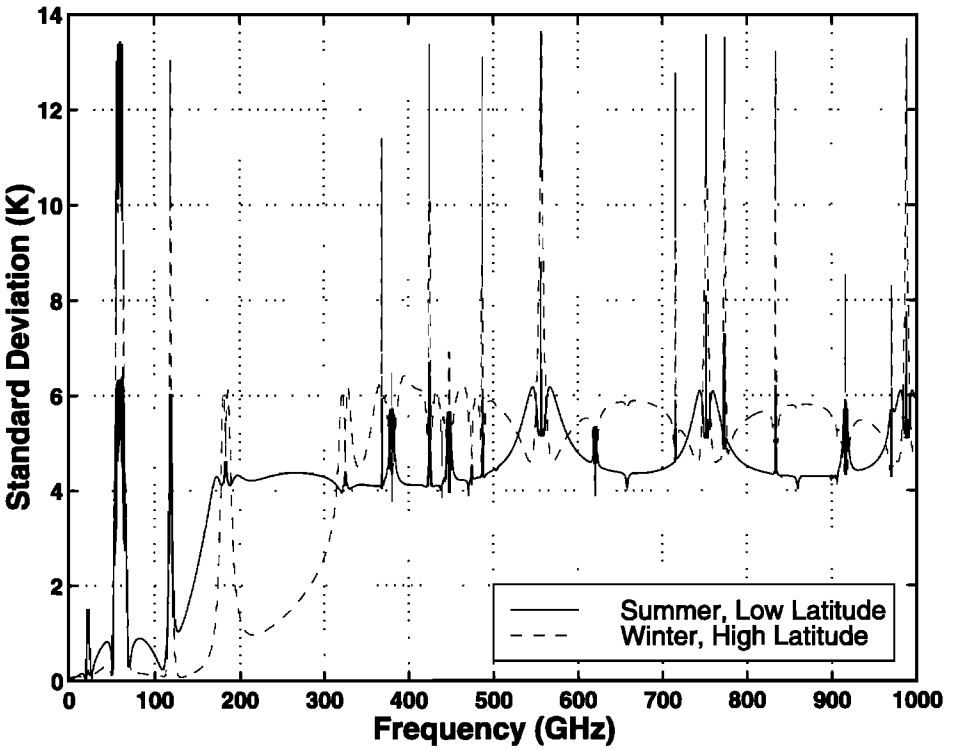

Figure 10. Standard deviation $\sigma_{TB,T}$ of upwelling brightness temperature due to the temperature variations for two extreme atmospheric profiles, nadir view over ocean background. Ozone influence is not considered.

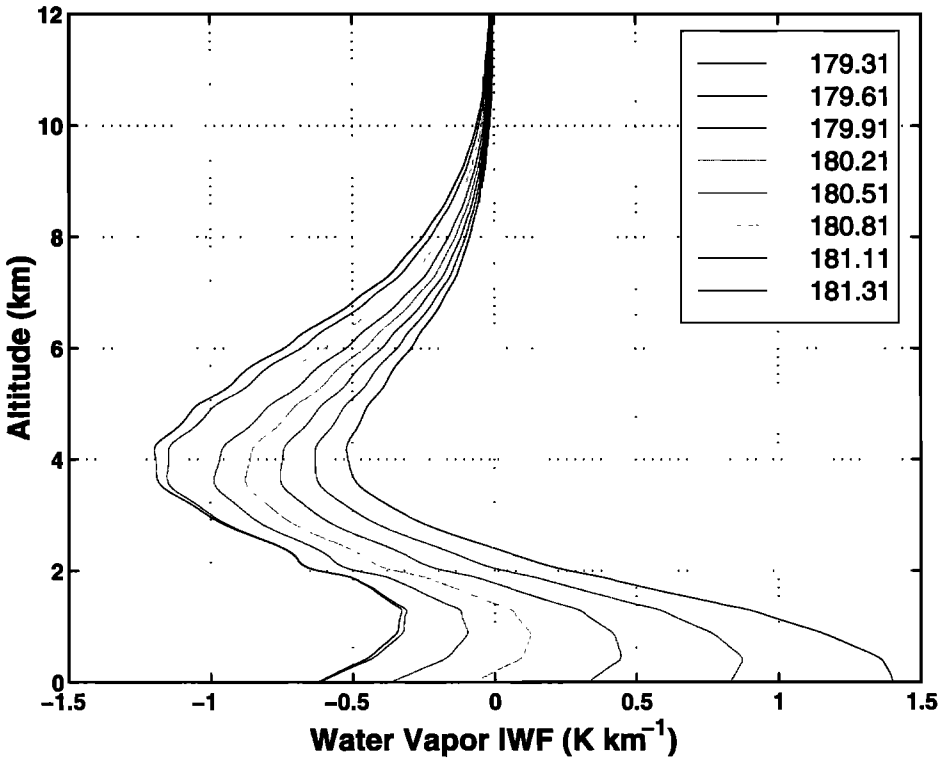

Figure 11. Water vapor IWF for single frequencies on the lower wing of the 183.3101 GHz absorption line for winter and high-latitude atmospheric conditions. Numbers in the legend are valid for curves from right to left.

Figures 12a-15a contains expanded plots of h_{eff} for the IWF along with the effective height standard deviation σ_h. Here σ_h is plotted only if the IWF has a distinct peak, as determined using the following half-power criterion:

$$\left|W_{p\text{MAX}}\right| \geq \frac{1}{\sqrt{2}} W_p(f,z,\theta)\Big|_{z=0}, \tag{22}$$

where $W_{p\text{MAX}}$ is the maximum absolute value of IWF for the given profile and frequency, and $W_p(f,z,\theta)\big|_{z=0}$ is the IWF value at the surface. The IWFs that do not satisfy condition (22) are considered to not have a distinct peak, and the standard deviation of their effective height is not computed. In the case of water vapor the IWF in (22) is multiplied by σ_ρ. At the centers of some absorption lines the σ_h for the water wapor IWF increases rapidly (e.g., Figure 13 (a2) for the 183.3101 GHz line or Figure 13 (a3) for the 325.1529 GHz line). This feature is caused by a secondary IWF peak at higher altitude that is not as well pronounced as the first one but is nonetheless strong enough to influence σ_h as defined by (22).

We can now define the natural available bandwidth B_N for a given frequency f as follows:

$$B_N = f_H - f_L \tag{23}$$

where

$$\begin{aligned} f_H > f \quad & h_{\text{eff}}(f_H) = h_{\text{eff}}(f) \pm \alpha\sigma_h(f), \\ f_L < f \quad & h_{\text{eff}}(f_L) = h_{\text{eff}}(f) \pm \alpha\sigma_h(f). \end{aligned} \tag{24}$$

Thus B_N is the bandwidth available for sounding provided that the effective height of the IWF over the contiguous band of width B_N is within limits determined by a fraction α of σ_h. In calculations of B_N we have excluded absorption by O_3 under the assumption (proven in section 6.5) that O_3 impact on the band-averaged IWF is mostly negligible. By the above definition the band of concern can be located on the side of a line or can include the line center (for H_2O lines), and the function B_N(f) can be discontinuous. The value of α selected for Figures 12c-15c is 0.25. Using this value of α insures that the IWF over the band of width B_N remains nearly as well peaked as a monochromatic IWF of the same frequency. For those points where σ_h is not defined (see (22)), B_N is not plotted (e.g., near the 22.2351 GHz absorption line in Figures 12 (c1) and 13 (c1)).

It is noted that by equations (23) to (24) the passband of width B_N at a given frequency is not necessarily symmetric about that frequency. This asymmetry is prominent for frequencies on the line wings where B_N can become quite large. For example, in Figure 12 (c2) the natural available bandwidth for the 183.3101 GHz water vapor line at +15 GHz offset (i.e., ~198 GHz) is seen to be ~100 GHz (that is, the band extends from ~193 to ~303 GHz). Although the band in this example is much wider than what can be practically allocated to passive sensing, B_N nonetheless represents a fundamental natural parameter of the terrestrial spectrum.

In Figures 12c and 13c many of the natural bands for water vapor sounding span the center frequencies of water vapor lines, thus including frequencies on both sides of the lines. One result is a discontinuity in B_N (visible in Figures 12 (c2)–12 (c10)), wherein (for example) in Figure 12 (c2) the bandwidths for frequency offsets within ~500 MHz of the center of the line are ~1 GHz, then decrease to ~700 MHz at

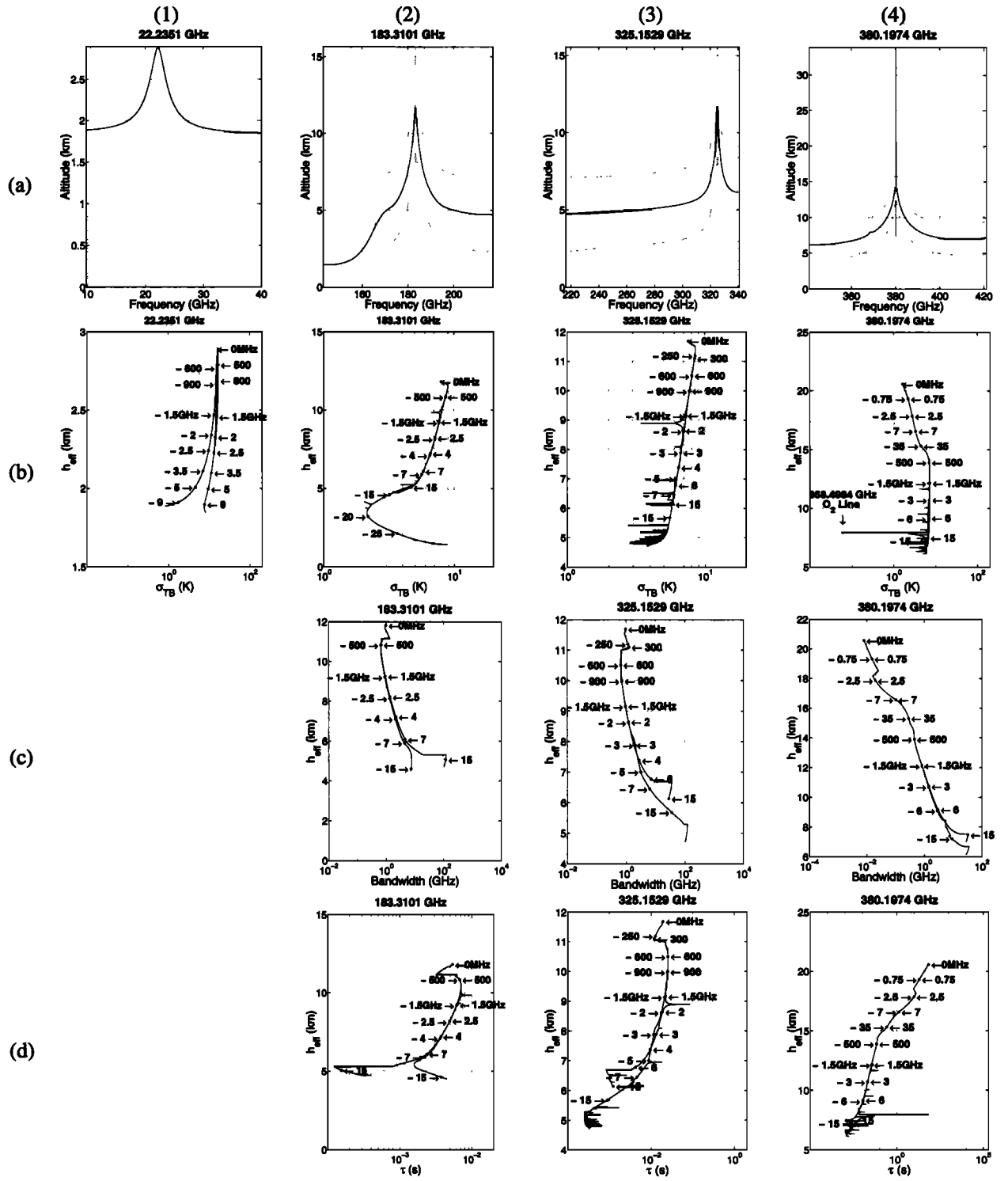

Figure 12. Water vapor sounding parameters near selected H_2O lines for summer and low-latitude conditions: (a) effective water vapor sounding height $h_{\mathrm{eff},\rho}$ (equation (17)) along with $h_{\mathrm{eff},\rho} \pm \sigma_{h,\rho}$ (equation (18)), (b) brightness standard deviation σ_{TB} (equation (21)) due to natural variations of water vapor, (c) natural available sounding bandwidth B_N (equations (23)-(24)), and (d) minimum integration time τ (equation (27)). Numbers are frequency offsets from the particular H_2O line center.

larger frequency offsets. The discontinuity occurs at the transition from using both wings of the line to using only one wing (on either side) of the line.

It is now useful to prescribe a minimum signal-to-noise ratio SNR_m necessary to sense natural brightness temperature variations in the presence of radiometer noise. Denoting the radiometer sensitivity as ΔT_{RMS} the minimum SNR becomes

$$\mathrm{SNR}_m = \left(\frac{\sigma_{TB}}{\Delta T_{\mathrm{RMS}}} \right)^2 . \tag{25}$$

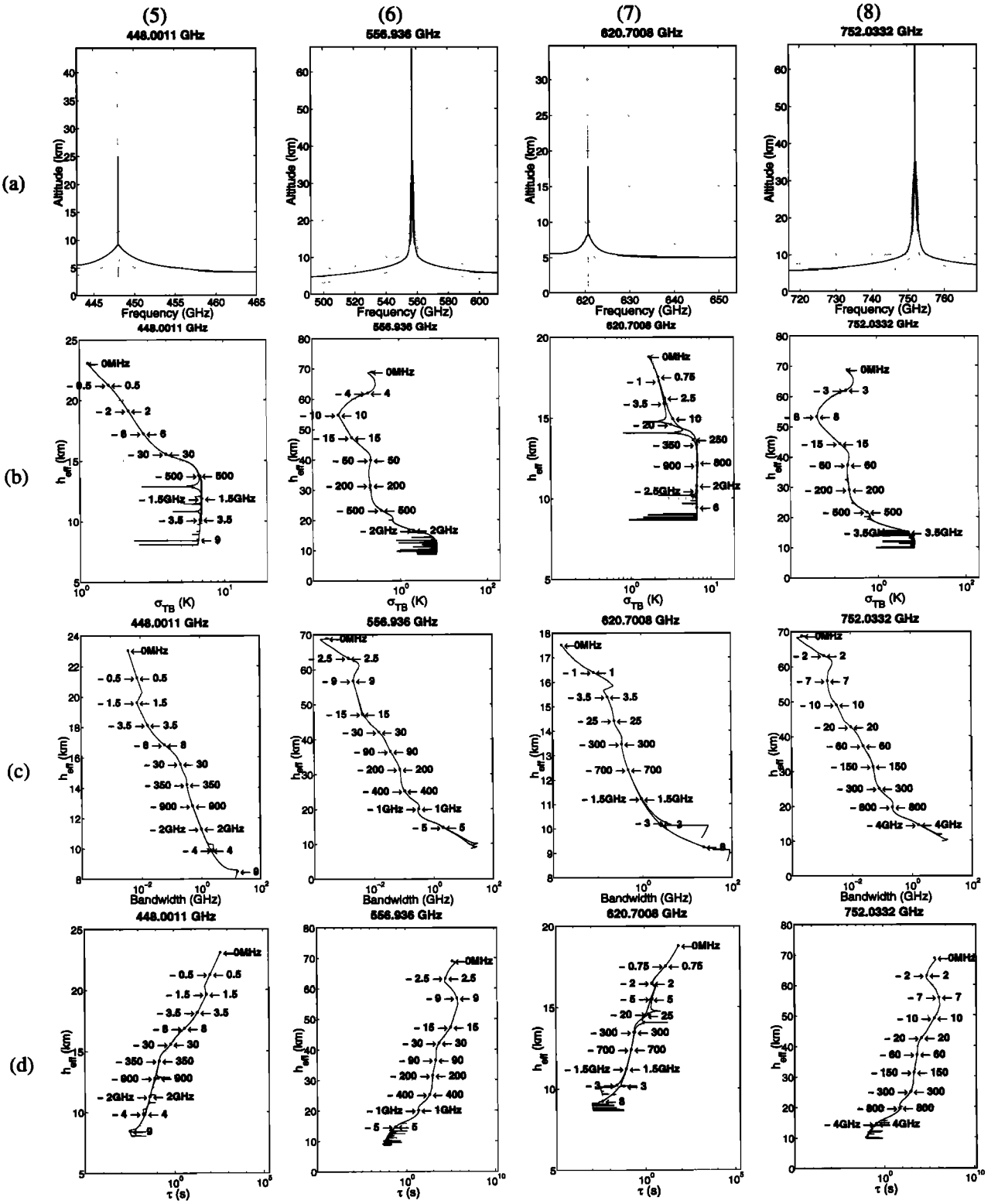

Figure 12. (continued)

Assuming a total power radiometer, ΔT_{RMS} is determined by the radiometer system noise temperature T_{SYS}, the channel bandwidth B, and the integration time τ by

$$\Delta T_{RMS} = \frac{T_{SYS}}{\sqrt{B\tau}}. \tag{26}$$

Accordingly, we can determine the minimum integration time τmin required for unambigious detection of natural atmospheric variations to be

$$\tau_{\min}(f) = \frac{T_{SYS}^2(f)\mathrm{SNR}_m}{B_N(f)\sigma_{TB}^2(f)}. \tag{27}$$

As an example, we have computed τmin in Figures 12d-15d for $\mathrm{SNR}_m = 100$ (i.e., 20 dB, or $\sigma_{TB} = 10\,\Delta T_{RMS}$) and $\alpha = 0.25$.

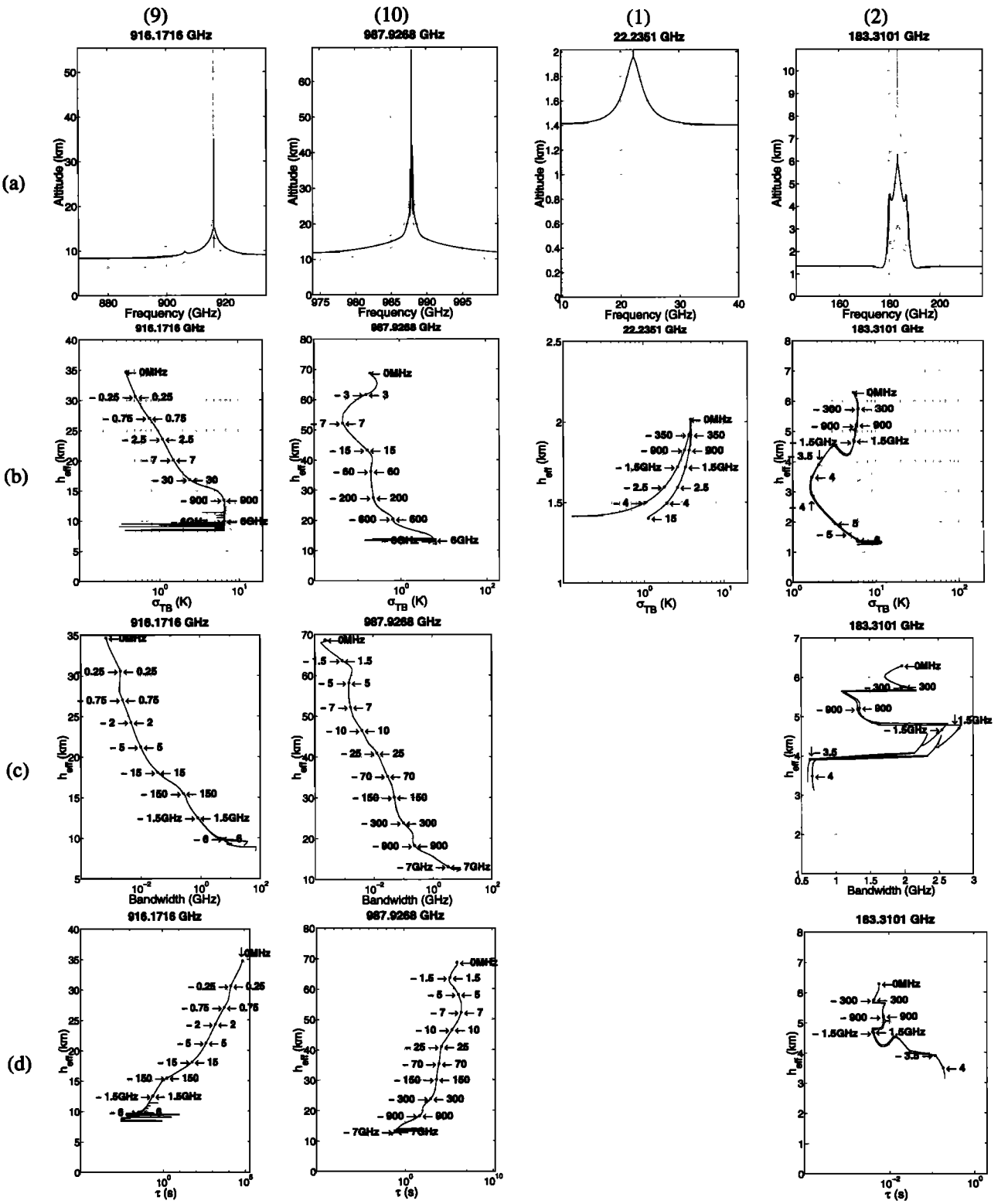

Figure 12. (continued)

In the above the double sideband system temperature T_{SYS} is conservatively modeled as [Staelin et al., 1997]

$$T_{SYS}(f)=\begin{cases}300\,\mathrm{K} & f<30\,\mathrm{GHz}\\ 10f\,\mathrm{K} & f>30\,\mathrm{GHz}\end{cases} \tag{28}$$

where f is in units of gigahertz. Although the above model is conservative, the derived values of τmin can be easily scaled

Figure 13. Water vapor sounding parameters near selected H_2O lines for winter and high-latitude conditions: (a) effective water vapor sounding height $h_{\mathrm{eff},\rho}$ (equation (17)) along with $h_{\mathrm{eff},\rho} \pm \sigma_{h,\rho}$ (equation (18)), (b) brightness standard deviation σ_{TB} (equation (21)) due to natural variations of water vapor, (c) natural available sounding bandwidth B_N (equations (23)-(24)), and (d) minimum integration time τ (equation (27)). Numbers are frequency offsets from the particular H_2O line center.

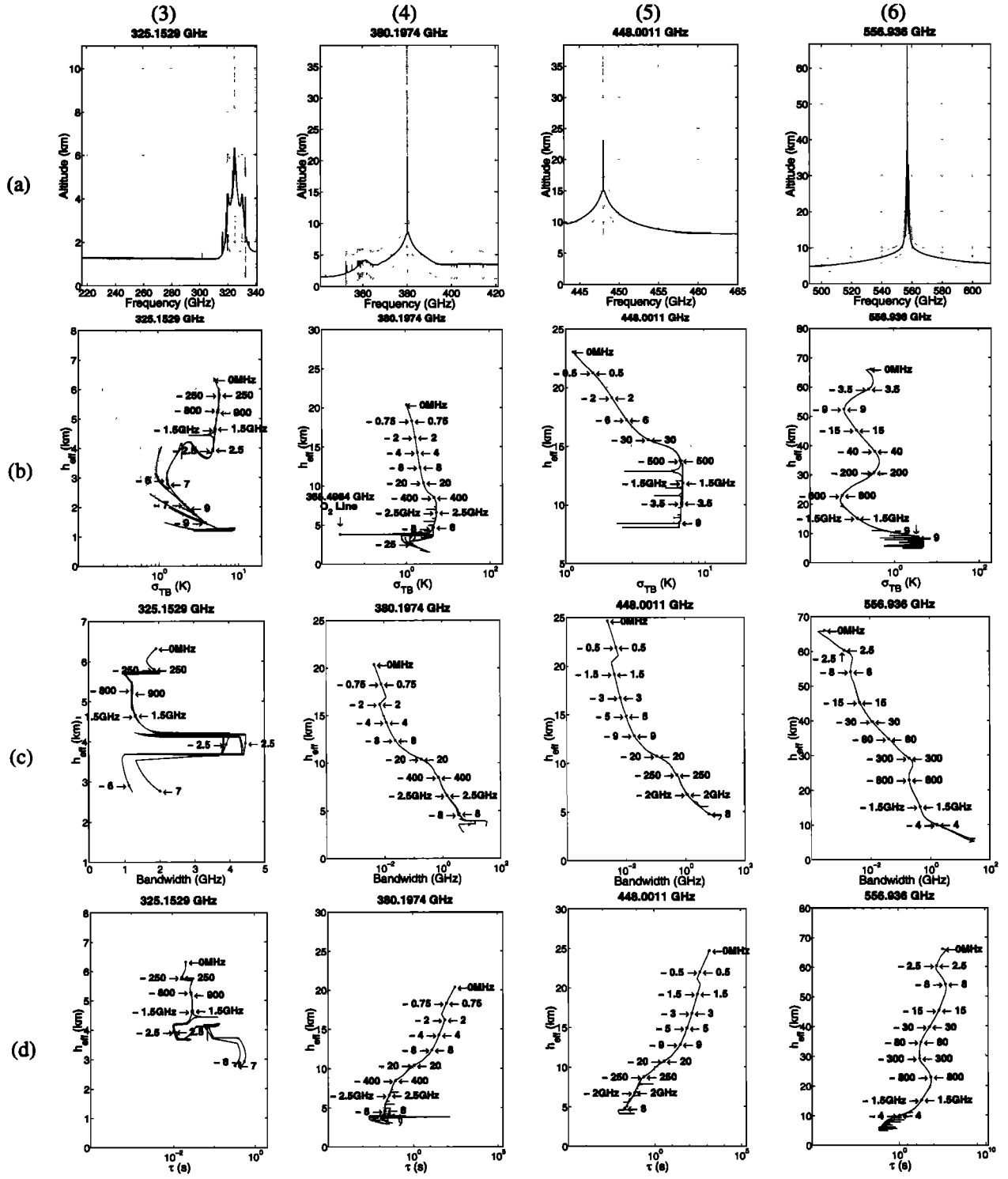

Figure 13. (continued)

to new values of T_{SYS} as receiver technology progresses. Given a value of α, SNR_m, and a receiver noise model, the above time τ_{min} is also fundamental in determining the nadir-sensing capabilities at any given frequency. It is noted that calculations of minimum integration time (Figures 12d and 13d) are impacted by the aforementioned discontinuity in B_N and thus also exhibit discontinuities near water vapor line centers.

6. Discussion

An overview of the anticipated sounding capabilities for the millimeter and submillimeter wave frequency range considered in this paper is shown in Figures 7 through 10 and summarized for several selected frequencies around the most significant water vapor and oxygen absorption lines in Tables 4 and 5. In these calculations the effects of ozone were

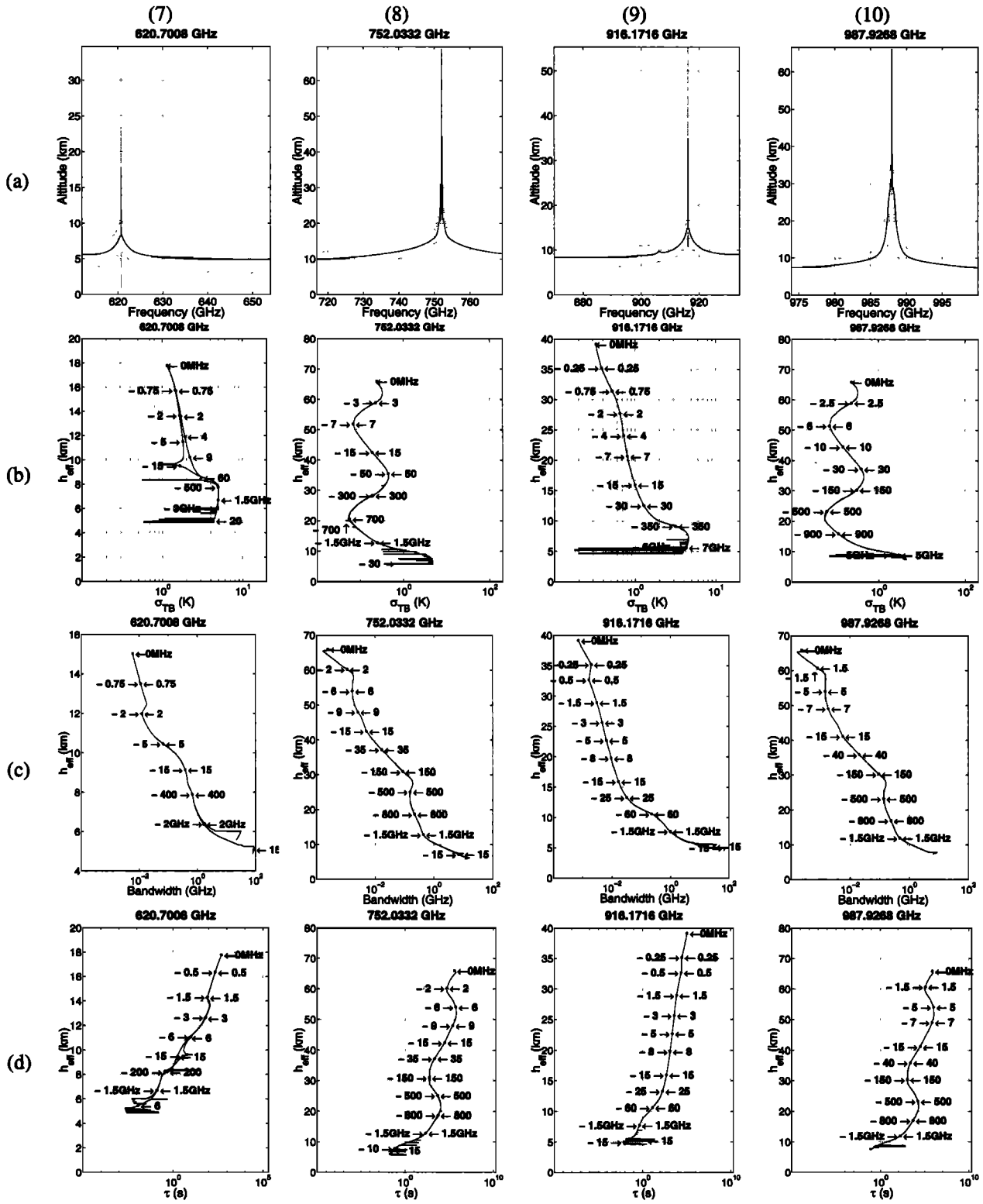

Figure 13. (continued)

excluded for clarity. Figures 12 through 17 show the sounding capabilities of selected ranges of frequency around several major water vapor and oxygen absorption lines, including the detailed effects of ozone. We discuss here what are perhaps the most significant of these lines for vertical sounding purposes.

Tables 4 and 5 summarize the sounding capabilities over ocean for several representative H_2O and O_2 sounding frequencies from 89 to 557 GHz. This range spans the frequency bands considered for use on the NASA/NOAA Advanced Geosynchronous Sensor satellite [*Adler*, 1998] and specifically includes frequencies allocated for passive sensing on either a primary or shared basis [*NTIA*, 1995]. For each frequency the effective sounding height h_{eff} is listed for the two extreme atmospheric conditions, along with natural available bandwidth B_N, minimum integration time τ_m, and

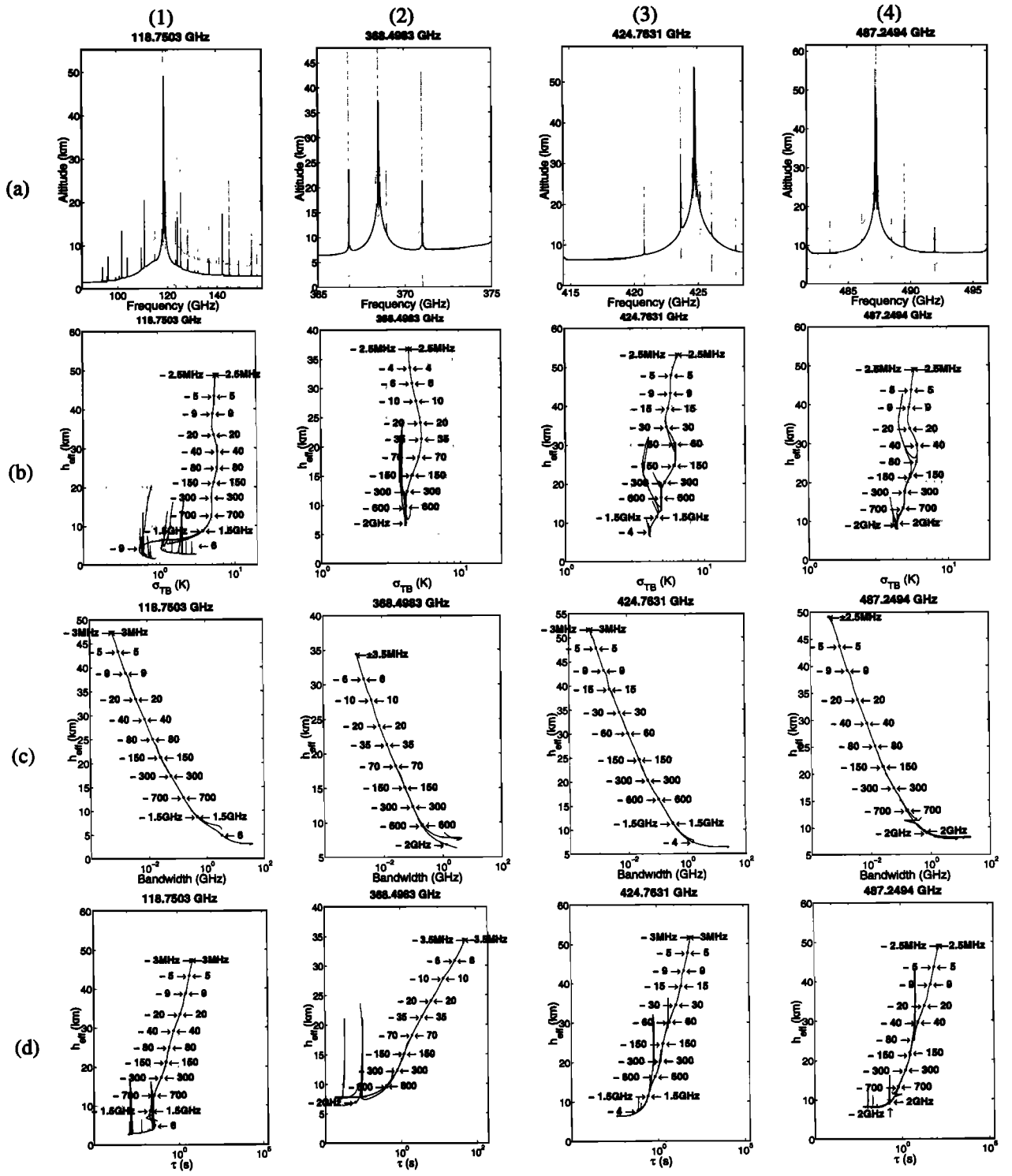

Figure 14. Temperature sounding parameters near selected O_2 lines for summer and low-latitude conditions: (a) effective temperature sounding height $h_{\mathrm{eff},T}$ (equation (19)) along with $h_{\mathrm{eff},T} \pm \sigma_{h,T}$ (equation (20)), (b) brightness standard deviation σ_{TB} (equation (21)) due to natural variations of temperature, (c) natural available sounding bandwidth B_N (equations (23)-(24)), and (d) minimum integration time τ (equation (27)). Numbers are frequency offsets from the particular O_2 line center.

subsatellite 3-dB footprint diameter assuming a circular uniformly illuminated aperture antenna on either a LEO or GEO sensor. For the LEO sensor a 0.5 m-diameter aperture at an altitude of 833 km (the Defense Meteorological Satellite Program (DMSP) orbital altitude) is assumed, and for the GEO sensor a 2-m-diameter aperture at an altitude of 35,782 km is assumed. Applications of these channels are discussed below.

6.1. Channels for Water Vapor Sounding

Seasonal and latitudinal varying amounts of moisture cause significant variations in water vapor sounding altitudes. For

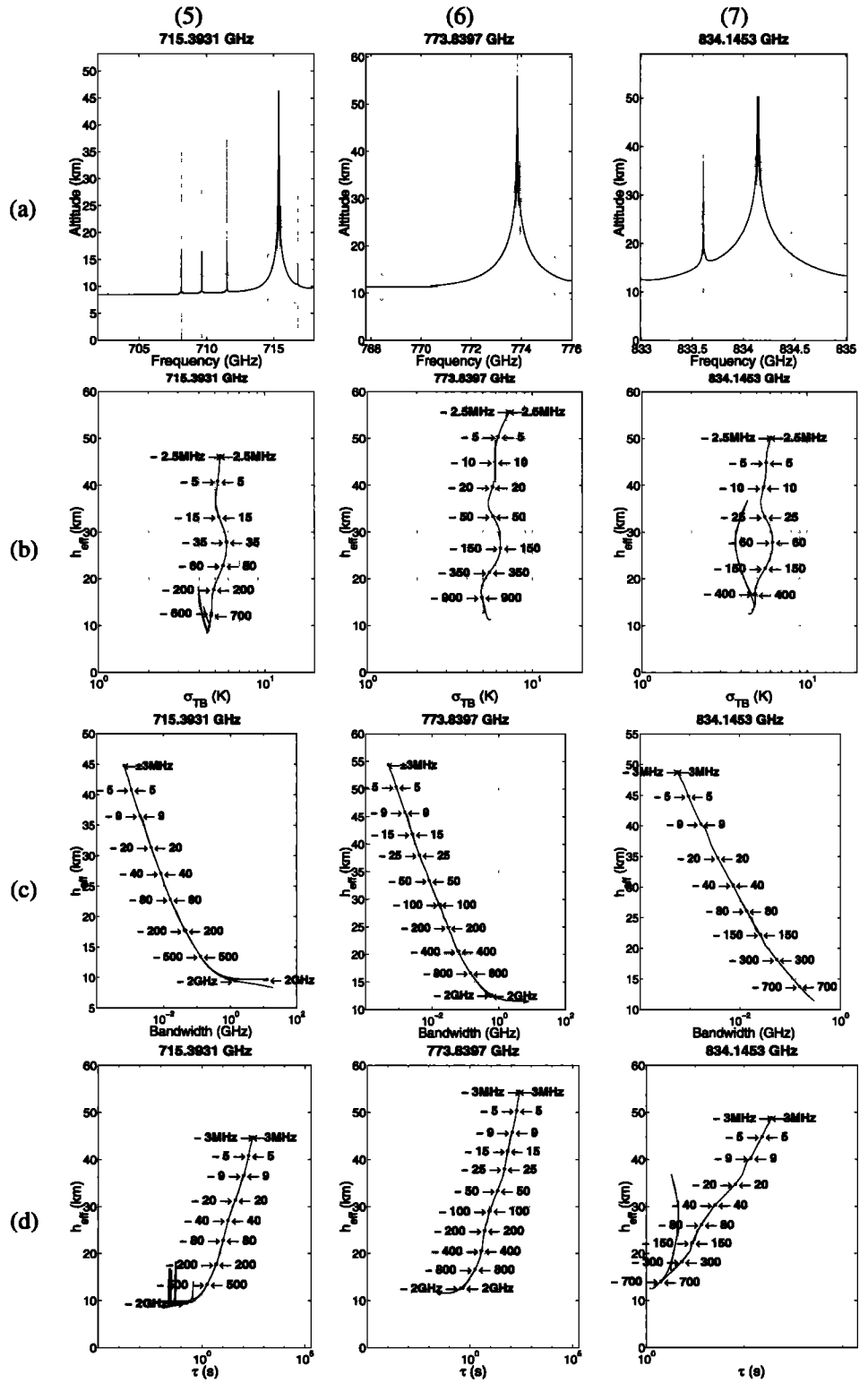

Figure 14. (continued)

the two extreme cases considered, the tropospheric vertical moisture content varies by more than 1 order of magnitude, resulting in the effective height for the same frequency varying by up to ~6 km. The variability of water vapor, along with the nonlinear relationship of the brightness temperature with moisture content indicates the necessity of nonlinear or geographically and seasonally indexed water vapor retrieval methods. The brightness temperature standard deviation σ_{TB} is also influenced by the season, latitude, and diurnal phase and must be similarly indexed within retrieval algorithms. We also note that water vapor sounding requires an accurate knowledge of the temperature profile around the altitude of interest and thus cannot practically be performed independent of temperature sounding.

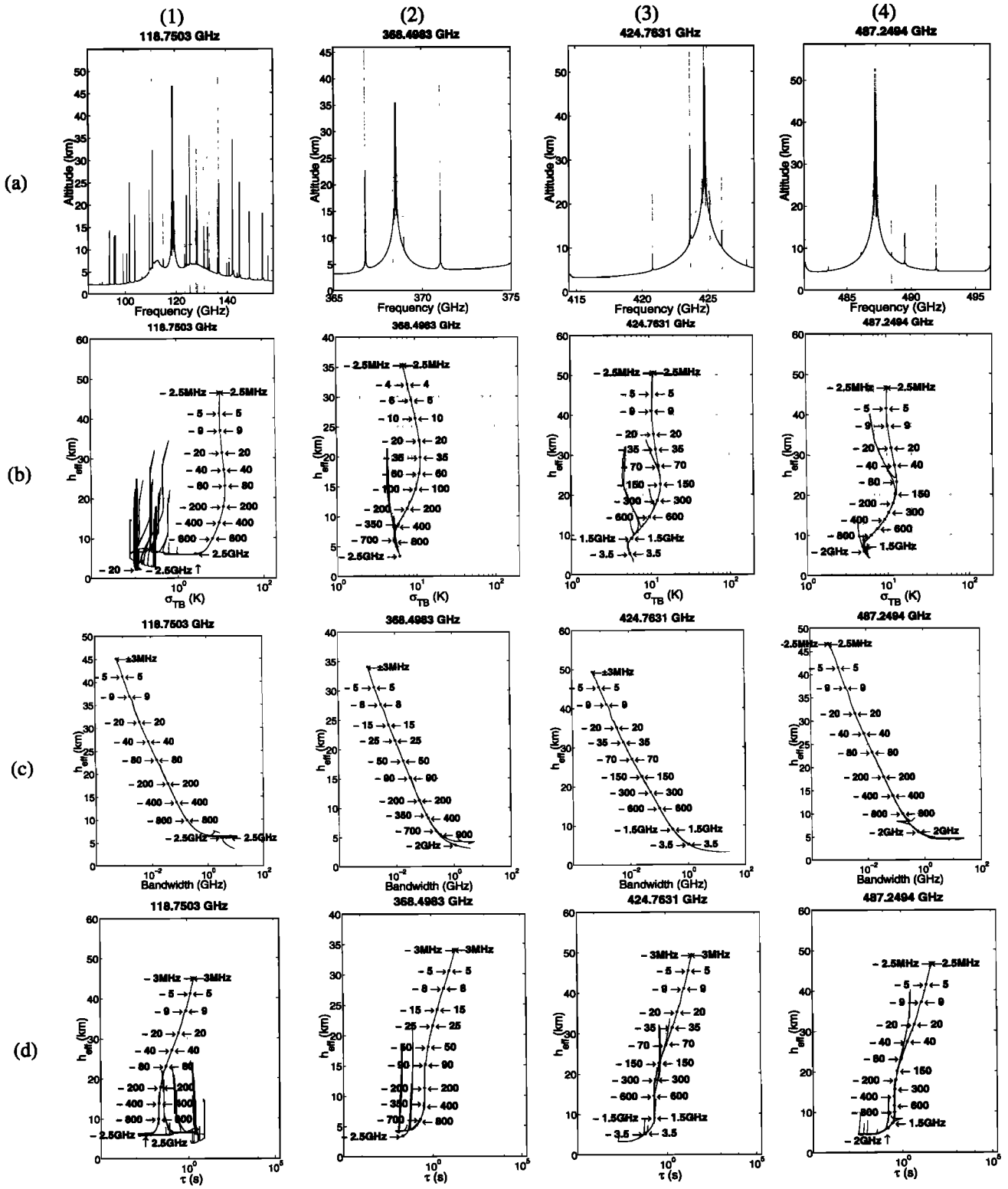

Figure 15. Temperature sounding parameters near selected O_2 lines for winter and high-latitude conditions: (a) effective temperature sounding height $h_{\mathrm{eff},T}$ (equation (19)) along with $h_{\mathrm{eff},T} \pm \sigma_{h,T}$ (equation (20)), (b) brightness standard deviation σ_{TB} (equation (21)) due to natural variations of temperature, (c) natural available sounding bandwidth B_N (equations (23)-(24)), and (d) minimum integration time τ (equation (27)). Numbers are frequency offsets from the particular O_2 line center.

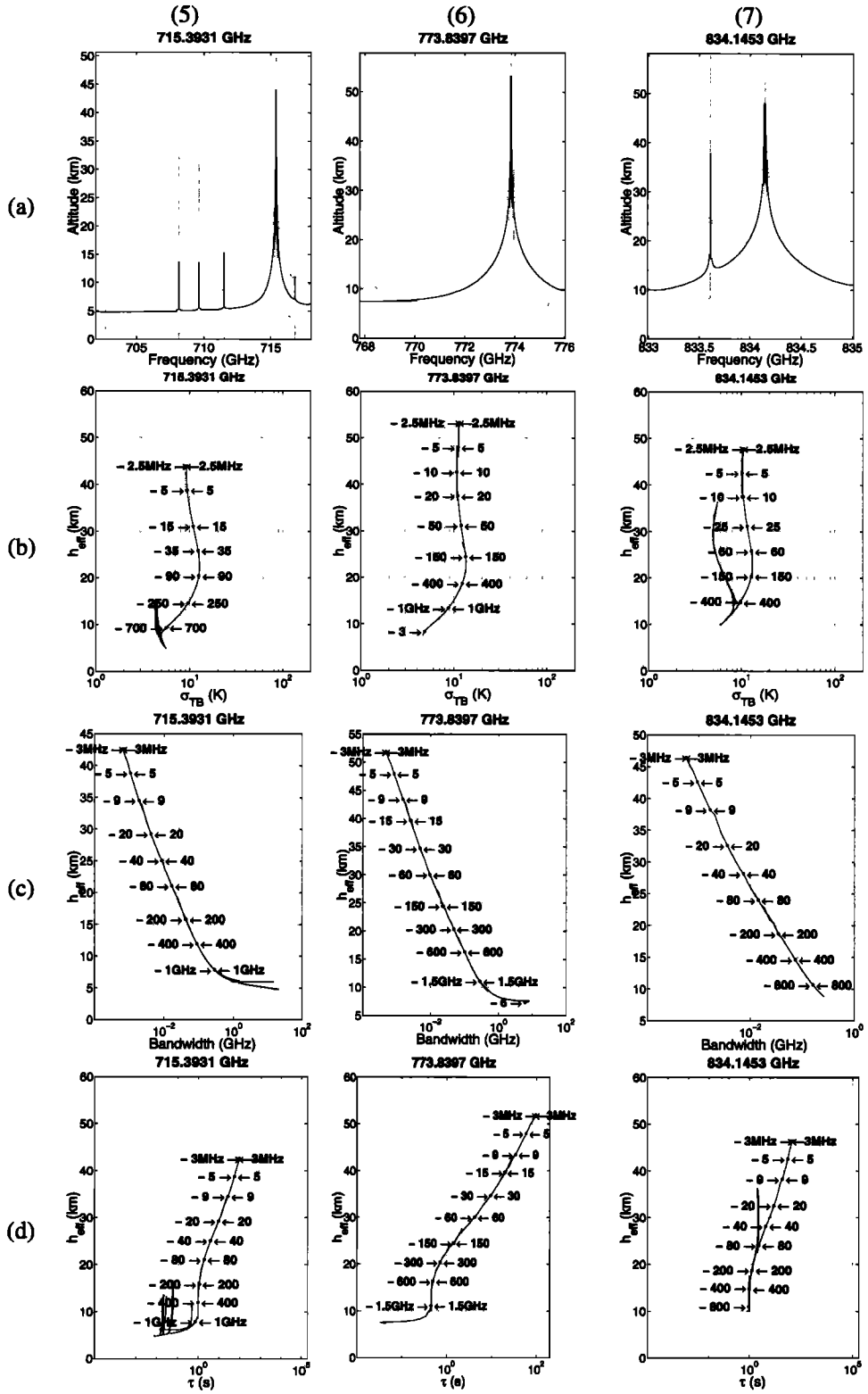

Figure 15. (continued)

The water vapor absorption lines at 325.1529, 380.1974, 448.0011, and 556.9360 GHz along with window channels in between them at ~318, ~341, ~410, and ~492 GHz are all good candidates for moisture sounding. The available effective sounding heights vary from a low of ~3 km for winter high-latitude conditions and ~6.5 km for summer tropical conditions to a high of ~60 km, although for altitudes above ~25 km, the minimum integration for sounding natural moisture variations becomes excessive (~1 hour or more; see section 6.2 below). None of these frequencies can directly probe emissions from the surface except under winter high-latitude conditions. For high-resolution water vapor sounding in the lower to middle troposphere it is thus necessary to use channels around the 183.3101 GHz line and in the window at

Table 4. Moisture Sounding Capabilities of Selected Window and Water Vapor Line Frequencies Over Ocean

f (GHz)	h_{eff} (Summer, Low Latitude) (km)	h_{eff} (Winter, High Latitude) (km)	B_N (MHz)	τ_{min} (s)	3 dB LEO Spot Size Diameter (km)	3 dB GEO Spot Size Diameter (km)	Relative Rayleigh Scattering Coefficient
89.0	2.4	1.9			7.15	76.98	1.0
141.8	1.9	1.8			4.49	48.31	6.4
151.0	2.2	1.8			4.21	45.37	8.3
166.0	4.8	1.8			3.83	41.27	12.1
180.3	7.7	4.6	7.7E+02	1.5E-02	3.53	38.00	16.8
182.3	9.9	5.3	3.7E+02	1.4E-02	3.49	37.58	17.6
183.1	11.4	6.0	3.7E+02	1.1E-02	3.48	37.42	17.9
219.3	5.0	1.7	8.5E+04	4.0E-04	2.90	31.24	36.9
318.2	6.5	3.0	3.0E+03	1.0E-02	2.00	21 53	163.3
322.2	7.9	4.1	1.0E+03	2.2E-02	1.98	21.27	171.7
324.2	9.8	5.3	3.7E+02	4.8E-02	1.96	21.14	176.0
325.0	11.3	6.0	3.7E+02	5.4E-02	1.96	21.08	177.8
341.5	6.2	2.2	2.1E+04	2.0E-03	1.86	20.06	216.8
373.2	8.7	5.0	1.7E+03	3 5E-02	1.71	18.36	309.2
377.2	10.7	6.3	7.0E+02	6.4E-02	1.69	18.16	322.6
379.2	12.8	7.8	3.0E+02	1.2E-01	1.68	18.07	329.5
380.2	18.0	15.4	4.0E+00	8.8E+01	1.67	18.02	333.0
410.2	7.0	4.0	2.3E+04	6.0E-03	1.55	16.70	451.3
441.0	9.0	5.1	2.0E+03	3.9E-02	1.44	15.54	602.8
445.5	10.4	6.1	7 3E+02	9.4E-02	1.43	15.38	627.8
447.0	12.6	7.7	2.8E+02	2.0E-01	1 42	15.33	636.3
448.0	18.7	16.6	3.5E+00	2.2E+02	1.42	15.29	642.0
492.5	8.6	4.9	1.1E+04	1.2E-02	1.29	13 91	937.7
540.0	11.9	7.4	3.7E+03	3.4E-02	1.18	12.69	1355.2
550.0	14 0	8.9	1.5E+03	2.2E-01	1.16	12 46	1458.4
554.0	15 8	10.8	5 0E+02	1.4E+01	1.15	12.37	1501.3
556.0	20.2	19 8	1.3E+02	6 6E+03	1 14	12.32	1523.1
556.7	32.2	31.4	4.0E+01	1.8E+03	1.14	12.31	1530.8
556.9	62.8	60.0	1.3E+00	4.6E+04	1.14	12.30	1533.0

Read 7.7E+02 as $7.7 \times 10^{+2}$.

~142 GHz (see 6.3 below), albeit with compromises in spatial resolution.

6.2. Stratospheric and Upper Tropospheric Water Vapor Sounding

As an example, consider first the sounding of water vapor in the middle-to-upper stratosphere between ~25 and ~45 km altitude. Using Figures 12a and 13a, we can determine suitable water vapor absorption lines by requiring that the range of effective sounding heights span these altitudes. In this case, lines at 556.9360, 752.0332, and 987.9268 GHz are suitable. Considering, for example, a nominal altitude of 35 km and using Figures 12b and 13b, it can be seen that for these three lines we require sounding frequencies that are approximately ±100, ±80, and ±80 MHz from the line centers, respectively. The variation of brightness temperature due to the natural variation of water vapor at these frequencies and altitudes is ~0.2 K for summer and low latitudes and ~0.3-0.4 K for winter and high latitudes, thus requiring exceptional radiometric stability and sensitivity, as well as extremely precise knowledge of the stratospheric temperature profile. The natural available bandwidth can be determined using Figures 12c and 13c to be ~20 MHz for all three lines and for both extreme atmospheric conditions. Assuming a total power radiometer and requiring an SNR of 20 dB, the necessary integration time would be ~10^3 to ~10^4 s, as determined from Figures 12d and 13d. Thus a state-of-the-art microwave radiometer for vertical sounding of natural moisture variations in the upper stratosphere would have to be geostationary to provide adequate sensitivity.

The reason that vertical sounding of upper stratospheric water vapor requires such large integration times is partly a result of the ratio of the natural variation of water vapor content to the mean water vapor content: this ratio is observed to drop to values considerably lower than unity for altitudes above ~20 km (see Figure 3), thus making natural variations difficult to observe. The reduction in the relative variation ratio in the middle and upper stratosphere is a consequence of stratification, and only large-scale pumping or drying of the upper stratosphere (caused, for example, by a major change in average tropospheric convection amount) could be expected to be observed by vertical sounding. The relatively small bandwidths required for upper stratospheric sounding also contribute to excessively long integration times. These

Table 5. Temperature Sounding Capabilities of Selected Windows and Oxygen Line Frequencies Over Ocean

f (GHz)	h_{eff} (Summer, Low Latitude) (km)	h_{eff} (Winter, High Latitude) (km)	B_N (MHz)	τ_{min} (s)	3 dB LEO Spot Size Diameter (km)	3 dB GEO Spot Size Diameter (km)	Relative Rayleigh Scattering Coefficient
89.0	2.5	3.0			7.15	76.98	1.0
111.8	5.9	7.8			5.69	61.28	2.5
115.8	7.5	6.6	2.2E+03	1.8E-02	5.50	59.16	2.9
117.8	11.2	9.1	2.7E+02	2.4E-03	5.40	58.16	3.1
118.7	44.8	42.8	1.1E+00	1.3E+00	5.36	57.72	3.2
341.5	5.0	3.1	2.1E+04	3.3E-03	1.86	20.06	216.8
362.5	5.9	3.4	4.4E+03	1.8E-02	1.76	18.90	275.2
365.5	6.4	3.8	1.2E+03	6.0E-02	1.74	18.74	284.4
367.5	8.0	5.6	3.8E+02	2.1E-01	1.73	18.64	290.7
368.5	34.3	32.5	1.7E+00	3 8E+01	1.73	18.59	293.9
407.2	6.0	3.5	1.9E+04	5.0E-03	1.56	16.82	438.2
417.8	6.5	4.2	4.2E+03	1.6E-02	1.52	16.40	485.6
421.8	8.3	6.2	9.0E+02	1.1E-01	1.51	16.24	504.5
423.8	13.6	11.4	1.8E+02	3.6E-01	1.50	16.17	514.1
424.8	48.5	46.2	1.0E+00	4.8E+01	1.50	16.13	519.0
464.2	7.1	3.9	1.1E+04	1.1E-02	1.37	14.76	740.0
480.2	7.6	4.3	5.9E+03	2.1E-02	1.33	14.27	847.5
484.2	8.2	5.2	1.4E+03	7.3E-02	1.31	14.15	876.1
486.2	11.5	8.9	2.3E+02	4.5E-01	1.31	14.09	890.6
487.2	45.1	43.1	1.1E+00	6.7E+01	1.31	14.06	898.0

integration times could be reduced somewhat by relaxation of the 20 dB SNR requirement, reducing the vertical resolution by widening the channel bandwidth beyond B_N, or designing the system only for observations of spuriously large variations in vapor. Clearly, other means of sounding water vapor at these altitudes (e.g., limb sounding, balloon-based sounding, or rocketsondes) would be more practical unless either the high spatial resolution of a vertical sounder or the identification of anomalously large upper stratospheric water vapor features were required.

In contrast, using the same methodology, we see that vertical sounding of upper tropospheric and lower stratospheric water vapor between ~10 and ~20 km altitude is feasible. Here lines at 380.1974, 448.0011, 556.9360, 620.7008, 752.0332, 916.1716, and 987.9268 GHz are suitable. The short integration times necessary for observations in the upper troposphere ($<10^{-1}$ s around 10-12 km altitude) suggest that imaging of water vapor in this altitude range using either a LEO or GEO system is practical. Although the rather large integration times required for the lower stratosphere (up to ~10^2 sec at ~20 km) preclude two-dimensional imaging of water vapor in this altitude range using a LEO system, either a GEO imager/sounder or fixed-beam LEO sounder for subtrack profiling could be used. Indeed, the importance of both upper tropospheric and lower stratospheric water vapor on the radiation balance of the Earth suggests that studying its spatial distribution with even a fixed-beam (nonimaging) LEO radiometer would be valuable.

6.3. Passive Frequency Allocations around 183 GHz

With regard to the 183.3101 GHz water vapor line it is noted that IWFs within the International Telecommunication Union (ITU) allocated frequency bands of 150-151 and 164-168 show distinct differences in their sounding heights (Figures 12a and 13a) and signs. These two channels are far enough apart from each other relative to their offset from the 183 GHz line center to warrant their simultaneous use for water vapor sounding, particularly if equivalent vertical sensitivity in both warm moist and cold dry climates is of concern. If one considers a progression of sidebands spaced at successive octaves from the 183.3101 GHz line center (and hence at progressively lower opacities) and starting with a 1 GHz offset, one obtains approximately the following sequence of offsets: 1, 3, 7, 17, and 33 GHz. These offsets coincide with 182, 180, 176, 166, and 150 GHz. Since the absorption at 150 GHz is close to the minimum absorption that occurs between 118 and 183 GHz, a set that includes both 150 and 166 GHz is warranted purely from the standpoint of being able to observe at a variety of well-distributed levels of opacity around the 183 GHz line, from that of near the line center to near the window minimum. The fact that current systems do not use both is a technological shortcoming that should be corrected in future systems using, for example, broadband monolithic microwave-integrated circuit (MMIC) receivers.

6.4. Channels For Temperature Sounding

Since oxygen is much more uniformly mixed in the atmosphere than water vapor, the seasonal and latitudinal variations in the effective sounding height for temperature are considerably smaller than for water vapor (Figure 8), and are effectively negligible. Indeed, most such variation in sounding height occurs for altitudes in the lower troposphere and is the result of water vapor absorption dominating the spectrum in the wings of the O_2 lines. Thus a similar situation to the above applies in that temperature sounding cannot

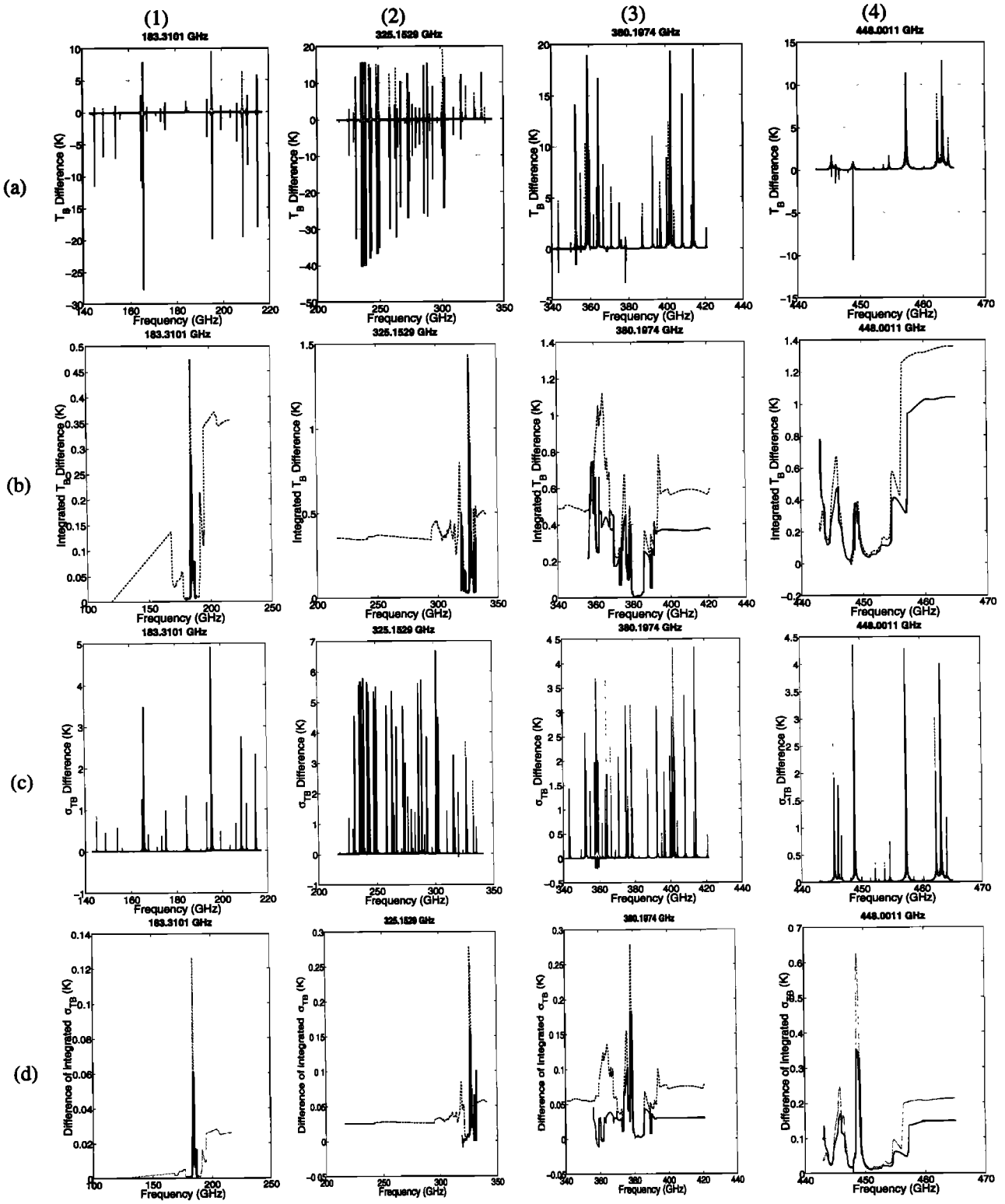

Figure 16. Influence of ozone on water vapor sounding for selected absorption lines: (a) T_B difference, (b) integrated T_B difference over the natural bandwidth B_N, (c) T_B standard deviation difference, and (d) integrated T_B standard deviation difference over the natural bandwidth B_N. The dotted line is for summer and low-latitude conditions, and solid line is for winter and high-latitude conditions.

practically be performed independent of water vapor sounding, particularly in the lower-to-middle troposphere.

From Table 5, suitable channel sets for temperature sounding are available around several O_2 lines or bands, including 50-70, 118.7503, 368.4983, 424.6891, and 487.2494 GHz. The corresponding sounding altitudes can range from near the surface to ~40 km. (Since Zeeman splitting is not included in the oxygen absorption model used in this study, temperature sounding at altitudes above ~40 km altitude is not considered here.) A significant difference exists

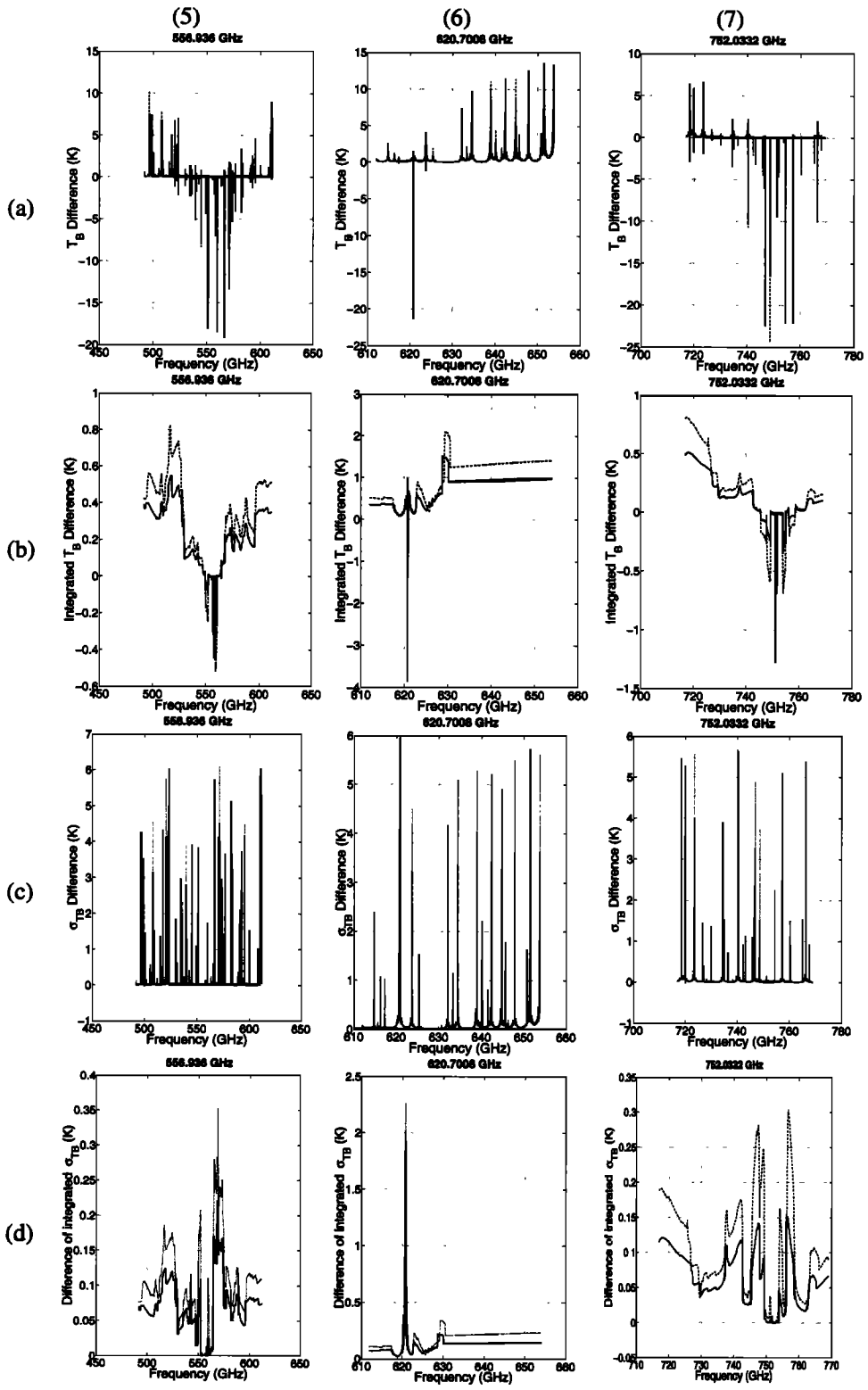

Figure 16. (continued)

in the frequency sensitivity of the effective height for water vapor and temperature sounding, with the greater sensitivity seen in the temperature sounding channels. One result of this difference is that the natural available bandwidth for temperature sounding channels is significantly smaller (by approximately 1 order of magnitude) than for water vapor channels of comparable sounding height. The channel bandwidths for stratospheric temperature sounding are restricted to only a few megahertz. The minimum integration times are, however, shorter than for water vapor sounding since $\sigma_{TB,T} >> \sigma_{TB,\rho}$.

Temperature sounding using the submillimeter wave O_2

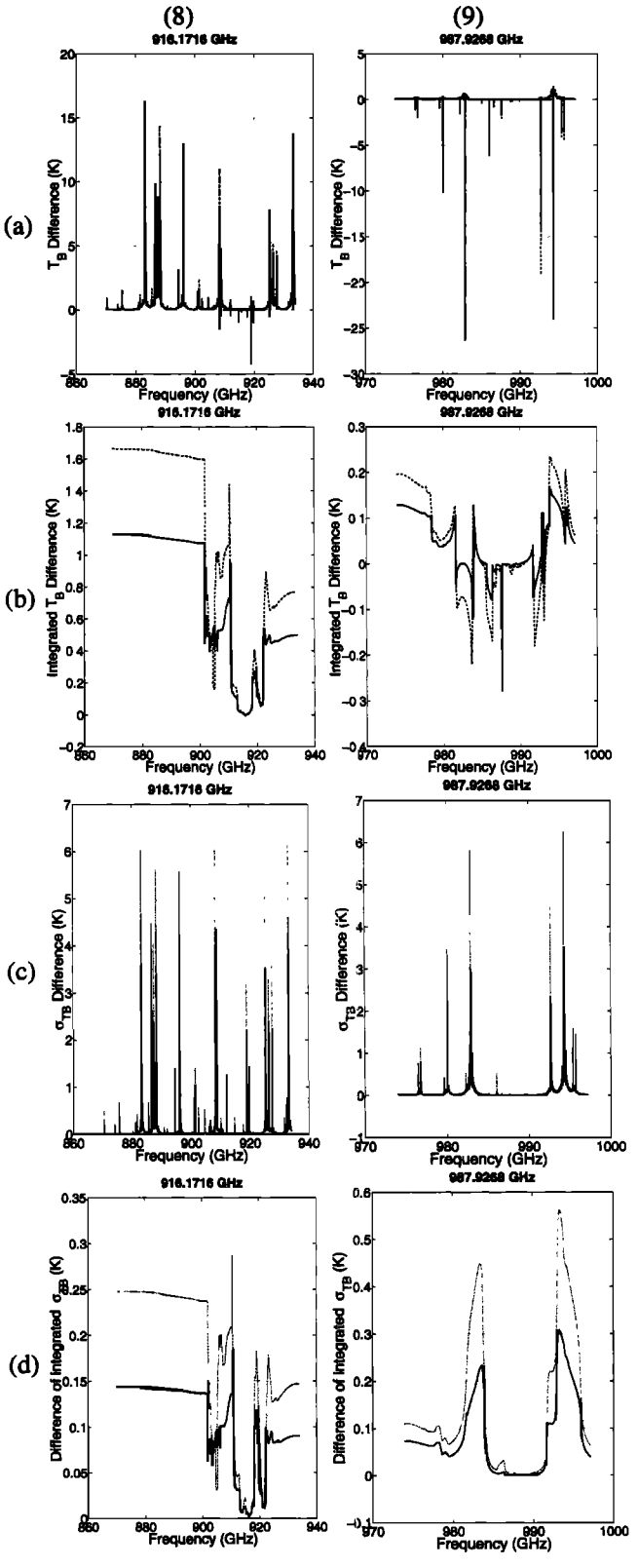

Figure 16. (continued)

lines at 368.4983, 424.6891, or 487.2494 GHz can provide considerably higher spatial resolution than that available using the 50-70 GHz band or the 118.7503 GHz line. Use of these submillimeter lines should include window channels at ~342, ~407, and ~464 GHz (respectively) to provide the best possible low-altitude sensitivity.

6.5. Effects of Stratospheric Ozone

The influence of ozone on temperature and water vapor sounding was studied by evaluating several key sounding parameters with and without absorption by ozone. Figures 16a and 17a show differences between brightness temperatures (T_B-T_{BO3}) evaluated for an ozone-free atmosphere (T_B) and for an atmosphere with an ozone profile as described below (T_{BO3}). The naturally occurring density of ozone is greatest in the stratosphere from ~15 to 35 km altitude and reaches partial pressures of ~5-15 mPa. We used the mean ozone profile from 42 selected TIGR profiles for both extreme atmospheric conditions in this study. Inclusion of ozone into the atmospheric model cools the brightness temperatures by up to 20 K at some frequencies but warms the brightness temperature by up to 40 K at others.

The perturbation from ozone is caused by two effects. First, in Figure 16 (a1) and 16 (a2) the entire T_B spectrum for summer and low latitudes (dotted curve) is higher for the case without ozone than with ozone. In this case the impact of ozone is to lift the peaking altitude of the (full) temperature weighting function higher in the troposphere. The negative vertical temperature gradient in the troposphere thus causes a cooler brightness temperature. For the winter high-latitude case, however, the brightness temperatures are warmer when ozone is included. This warming is surface dependent. For an ocean background the brightness temperatures include a cold sky component reflected from the water surface, the impact of which diminishes when viewed through a relatively warm ozone layer. When there is greater attenuation in the atmosphere (due to, for example, ozone), the cold reflected radiation becomes dominated by warm (directly emitted) radiation. A second cooling mechanism is apparent in Figures 16 (a3)-16 (a9), where a negative brightness perturbation is seen in the vicinity of strong water vapor or oxygen absorption lines. This cooling effect is the result of an increase in the peaking altitude of the full weighting function into the stratosphere, wherein the positive temperature gradient of the stratosphere produces an overall warming in brightness.

In an analogous fashion, Figures 16c and 17c show standard deviation differences σ_{TB} - σ_{TBO3} as defined by equation (21). The differences indicate significant reductions (up to 5-7 K) in the geophysical variance of the brightness spectra around ozone lines. Note that in a few special cases the T_B variance actually increases when ozone is added. This unusual condition is the result of vertical anticorrelation in either temperature or humidity variations (as described by the respective covariance matrix) along with a shift in the peaking altitude of the respective incremental weighting functions when ozone is considered. In most cases, however, the natural variance of the brightness decreases.

While the perturbation spectra in Figures 16a and 17a show rather large deviations in comparison with the precision required for most sounding applications, the situation is seen to be less critical when one considers the width of bands that can be used for water vapor and temperature sounding. Figures 16b and 17b show the above perturbations integrated over the natural available bandwidth B_N, namely,

$$\frac{\int_{f_1}^{f_2}(T_B - T_{BO3})df}{B_N}, \tag{29}$$

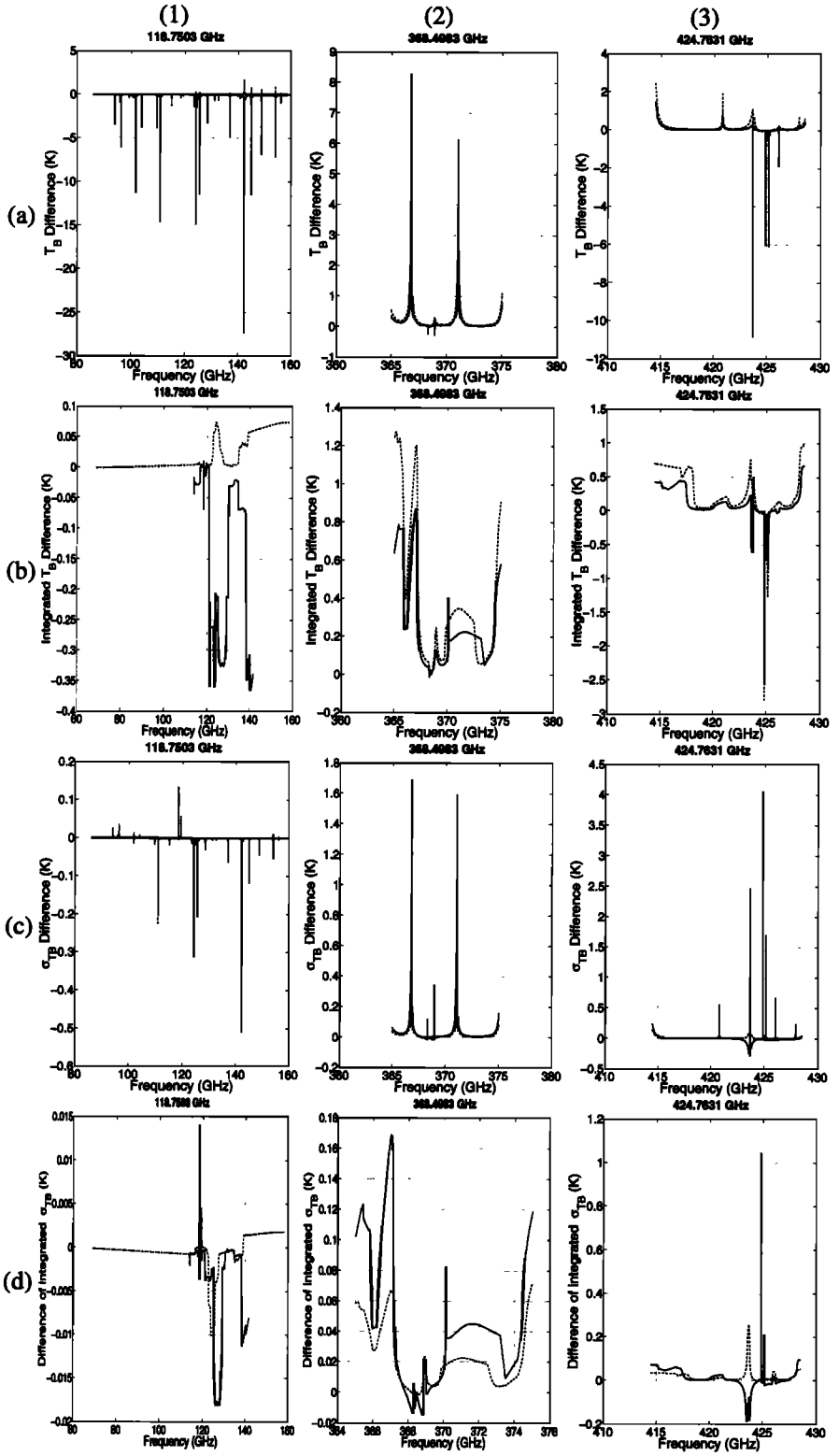

Figure 17. Influence of ozone on temperature sounding for selected absorption lines: (a) T_B differences, (b) integrated T_B difference over the natural bandwidth B_N, (c) T_B standard deviation difference, and (d) integrated T_B standard deviation difference over the natural bandwidth B_N. The dotted line is for summer and low-latitude conditions, and solid line is for winter and high latitude conditions.

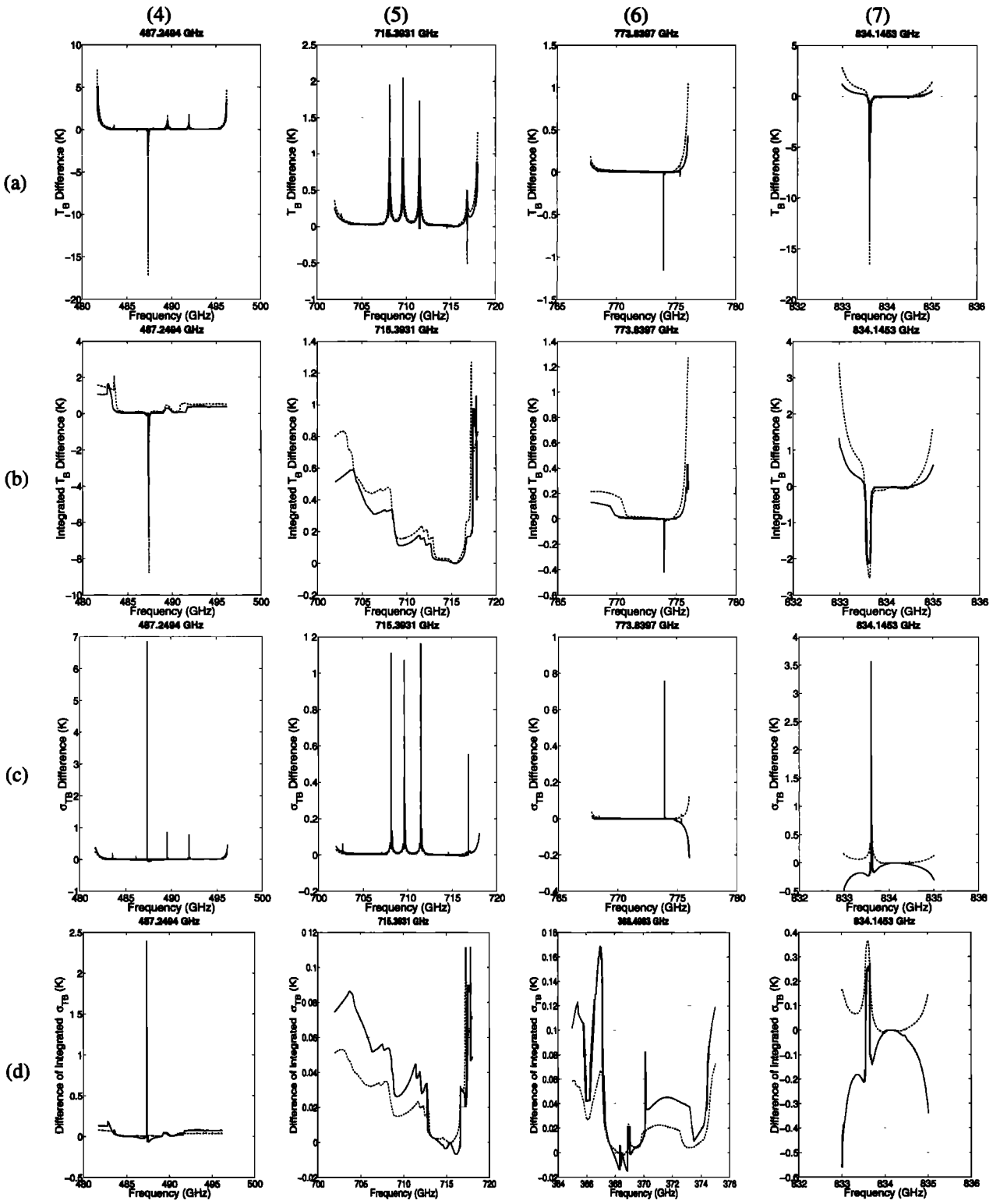

Figure 17. (continued)

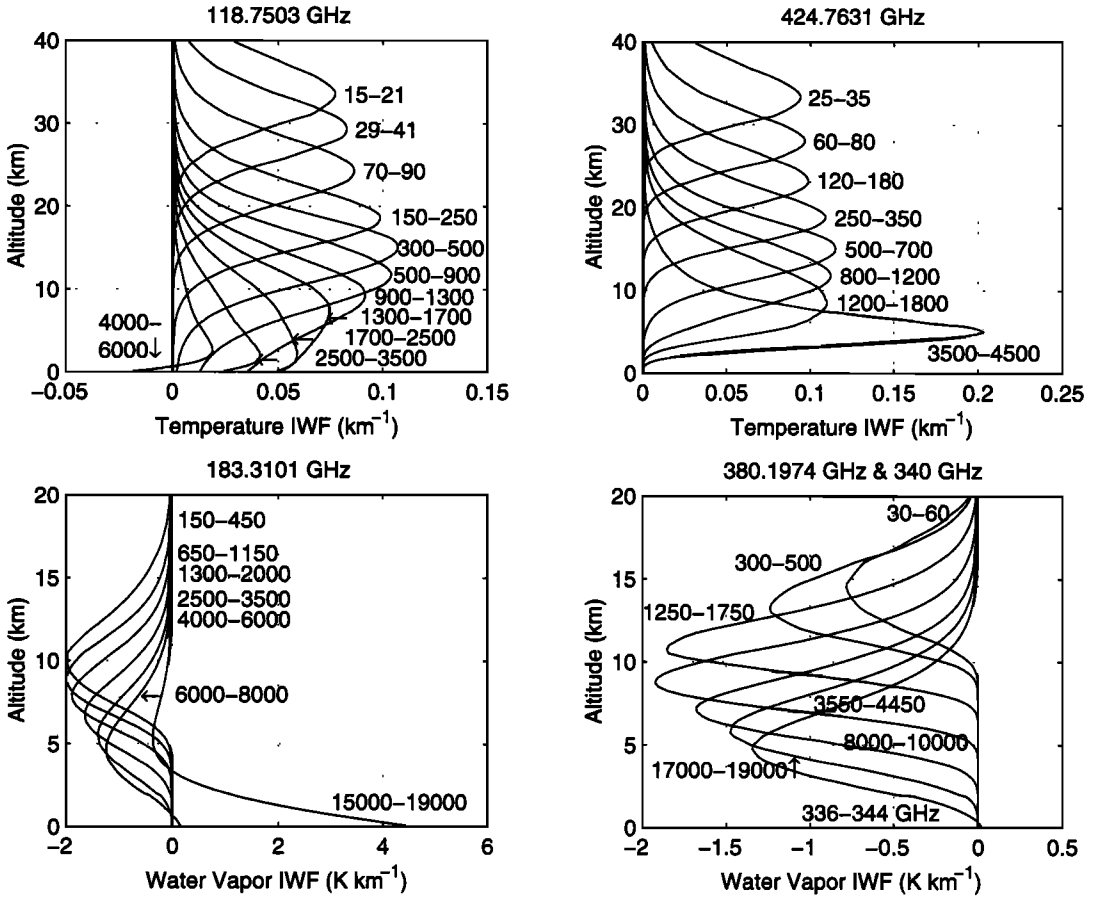

Figure 18. Proposed channels for a geosynchronous microwave sounder. Numbers show the frequency offset (in megahertz) from the center of absorption line.

where f_1 and f_2 are the endpoint frequencies of the band of width B_N, respectively. Analogously, Figures 16d and 17d show standard deviations differences $\sigma_{TB} - \sigma_{TBO3}$ integrated over the naturally available bandwidth B_N:

$$\sqrt{\frac{\int_{f_1}^{f_2}\left(\sigma_{TB}^2\right)df}{B_N}} - \sqrt{\frac{\int_{f_1}^{f_2}\left(\sigma_{TBO3}^2\right)df}{B_N}}. \tag{30}$$

One sees from the calculations that the bandwidth-averaged brightness perturbations are at maximum 2 K and typically less than 0.5-1 K. Also, the bandwidth-averaged standard deviation differences are at most 3 K and typically less than 0.5 K. The impact of absorption by upper tropospheric and stratospheric ozone on water vapor sounding is thus seen to reduce the sensitivity to low-altitude water vapor and temperature and moisture variations but only over spectral intervals much narrower than those typically encountered in sounding. These specific intervals can be identified by the wisp-like spikes in Figures 12b, 13b, 14b, 15b, and 12d, 13d, 14d, and 15d. At most, the screening effects of ozone lines are moderate and warrant no special concern unless the sensing bandwidth is restricted below B_N for either technological or spectral allocation reasons.

Stratospheric ozone also impacts temperature sounding by slightly increasing IWF sensitivity in the stratosphere. The amount of increase is variable (depending on the O_3 density), but for the strongest ozone lines can be expected to cause a complete shift of the support of the IWF to the stratosphere or even mesosphere. The shifts are evident as groups of filament-like excursions in the plots of σ_{TB} versus h_{eff} (Figures 14b and 15b) and are more prevalent away from the O_2 line centers. Such excursions will occur over relatively narrow sounding bands; over bands of width B_N (or comparable) the stratospheric sensitivity effects of ozone absorption are again negligible.

6.6. Geosynchronous Sounding and Imaging

An equatorial spatial resolution of ~20 km or better can be obtained from geosynchronous orbit using channels above ~320 GHz with apertures of moderate size (~2 m diameter). Such resolution is adequate for a variety of synoptic applications, including mapping of severe weather (i.e., convection, hurricane rainbands and eyewall locations, and fronts), nowcasting and forecasting, atmospheric dynamics research, and numerical weather prediction (NWP) model initialization [*Staelin et al.*, 1997]. Some additional improvements in resolution (by ~15-25%) can be expected using antenna pattern deconvolution techniques. To obtain comparable resolution using, for example, the 183.3101 GHz H_2O absorption line the required geosynchronous aperture diameter increases to ~4 m. Since sensor cost is driven to a large extent by aperture size, varying roughly as size to the third power, the cost savings available using higher sounding frequency lines is considerable.

For geosynchronous sounding and imaging it is suggested that a suite of several channels around the following window, water line, and oxygen line frequencies would provide good vertical coverage from the surface to the lower stratosphere with good spatial resolution down through the middle troposphere. A combination of channels at the 118.7503 and 424.7631 GHz lines provides vertical temperature coverage nearly comparable to that of the 50-60 GHz band, but with spatial resolution adequate for GEO imaging and observable degrees of freedom related to cloud absorption and scattering. Similarly, a combination of channels at the 183.3101 GHz water vapor line and another submillimeter wave water vapor line provides adequate vertical water vapor coverage, useful GEO spatial resolution, and additional spectral degrees of freedom necessary to compensate water vapor soundings for clouds: (1) 118.7503, 150, 166, 183.3101 GHz (for cloud penetrability, temperature and water vapor profiling, and water vapor observational heritage); (2) {220, 325.1529} or {340, 380.1974} or {410, 448.0011 GHz} (for cloud detection and high spatial resolution); The 380.1974 or 448.0011 GHz lines could provide unique upper troposphere/lower stratosphere water vapor sensitivity); (3) 410, 424.7631 GHz (for temperature profiling and high spatial resolution rain cell mapping). The IWFs for such a candidate set of channels useful for geosynchronous sounding in summer midlatitude conditions are shown in Figure 18. The additional degrees of observational freedom are expected to facilitate unified sounding of temperature and water vapor along with clouds and some partially transparent precipitation.

The addition of several channels in the vicinity of the 556.9360, 752.0332, and 987.9268 GHz water vapor lines could provide better high-altitude cirrus cloud detectability and the capability for middle-to-upper stratospheric water vapor sounding but (for reasons cited above in section 6.2.) at considerably lower temporal (or equivalently, spatial) resolution. The mapping of deeply convective storm tops, however, would require approximately 2 orders of magnitude less radiometric precision (i.e., ~1-2 K sensitivity), and hence almost 4 orders of magnitude less integration time. The available improvements in spatial resolution for images of severe weather using these channels might therefore warrant their inclusion; the problem of submillimeter wave cloud and raincell imaging is currently being addressed in a separate study.

Acknowledgments: The authors acknowledge support from NASA Headquarters through grant NAG5-1490 and the NOAA National Environmental Satellite Data and Information Service (NESDIS) through the Advanced Geosynchronous Studies (AGS) program. During part of this work the first author (Klein) was supported under a Fulbright fellowship. Several constructive comments from the reviewers are also appreciated.

References

Adler, R. F., Science Benefits of Advanced Geosynchronous Observation, NASA Goddard Space Flight Cent., in press, 1998.

Birnbaum, G., B. Guillot, and S Bratos, Theory of collision-induced lineshapes-absorption and light scattering at low density, *Adv. Chem. Phys., 51*, 49-112,1982.

Chedin, A., N.A. Scott, C. Wahiche, and P. Moulinier, The improved initialization inversion method, A high resolution physical method for temperature retrievals from satellites of the TIROS-N series, *J Clim. Appl. Meteorol., 24*, 128-143, 1985.

Cheury, F., F. Chevallier, N.A. Scott, A. Chedin, A new generation of radiative transfer models for climate studies based on neural networks, in *1995 IEEE International Geoscience and Remote Sensing Symposium Proceedings, IGARSS'95*, vol.1, pp. 535-537, IEEE Press, Piscataway, N. J., 1995.

Dagg, I. R., G.E. Reesor, and J.L. Urbaniak, Collision induced absorption in N_2, CO_2, and H_2 at 2.3 cm^{-1}, *Can. J. Phys., 53*, 1764-1776, 1975.

Dagg, I. R., G.E. Reesor, and M. Wong, A microwave cavity measurements of collision-induced absorption in N_2 and CO_2 at 4.6 cm^{-1}, *Can. J. Phys., 56*, 1037-1045, 1978.

Evans, K. F., A.H. Evans, I.G. Nolt, and B. T. Marshall, The prospect for remote sensing of cirrus clouds with a submillimeter-wave spectrometer, *J. Appl. Meteorol., 38* (5), 514-525, 1999.

Francois, C., and C. Ottle, Atmospheric corrections in the thermal infrared, global and water vapor dependent split-window algorithms-applications to ATSR and AVHRR data, *IEEE Trans. Geosci. Remote Sens., 34*, (2), 457-470, 1996.

Gasiewski, A. J., Numerical sensitivity analysis of passive EHF and SMMW channels to tropospheric water vapor, clouds, and precipitation, *IEEE Trans. Geosci. Remote Sens., 30* (5), 859-870, 1992.

Gasiewski, A. J., Microwave radiative transfer in hydrometeors, in *Atmospheric Remote Sensing by Microwave Radiometry* edited by M.A. Janssen, chap. 3, John Wiley, New York, 1993.

Gasiewski, A. J., and D.H. Staelin, Numerical modeling of passive microwave O_2 observations over precipitation, *Radio Sci., 25* (3), 217-235, 1990.

Isemer, H. J., A.F. Bunker,and L. Hasse, *The Bunker Climate Atlas of the North Atlantic Ocean*, Springer-Verlag, New York, 1985.

Klein, M., and Gasiewski, A. J., Sensitivity of millimeter and submillimeter wave channels to clear air temperature and water vapor variations, *NOAA Tech. Memo. ERL ETL-292*, Natl. Oceanic and Atmos. Admin. Boulder, Colo., 1998.

Liebe, H. J., An atmospheric millimeter wave propagation model, *NTIA Rep. 83-137*, U.S. Dep. of Comm., Washington, D.C., 1983.

Liebe, H. J., A contribution to modeling atmospheric millimeter-wave properties, *Frequenz, 41*, (1-2), 31-36, 1987.

Liebe, H. J., G.A. Hufford, and R.O. DeBolt, The atmospheric 60-GHz oxygen spectrum: Modeling and laboratory measurements, *NTIA Report 91-272*, U.S Dep. of Comm, Washington, D. C.,1991.

Liebe, H J., G.A. Hufford, and M. G. Cotton, Propagation modeling of moist air and suspended water/ice particles below 1000 GHz, paper presented at the AGARD Fifty-second Special Meeting of the Panel on Electromagnetic Wave Propagation, Advis. Group Aerosp. Res. Dev., Palma De Malorca, Spain, May 17-21, 1993.

National Telecommunication and Information Administration (NTIA), Tables of frequency allocation and other extracts from: Manual of Regulations and Procedures for Federal Radio Frequency Management, U.S. Dep. of Comm., Washington, D. C., 1995.

Phalippou. L., Variational retrieval of humidity profile, wind speed, and cloud liquid water path with the SSM/I: Potential for numerical weather prediction, *Q. J. R. Meteorol. Soc., 122*, 530, 327-355, 1996.

Poynter, R. L., and H.M. Pickett, Submillimeter, millimeter, and microwave spectral line catalog, *Appl. Opt., 24* (14), 2235-2240, 1985.

Rosenkranz, P. W., Absorption of microwaves by atmospheric gases, in *Atmospheric Remote Sensing by Microwave Radiometry*, edited by M.A. Janssen, pp.37-90, John Wiley, New York, 1993.

Rosenkranz, P. W., Water vapor microwave continuum absorption: A comparison of measurements and models, *Radio Sci., 33* (4), 919-928, 1998.

Russel, J.M., III, L. L. Gordley, J. H. Park, S. R. Drayson, W. D. Hesketh, R. J. Cicerone, A. F. Tuck, J. E. Frederick, J. E. Harries, and P. J. Crutzen, The Halogen Occultation Experiment, *J. Geophys. Res., 98*, 10777-10797, 1993.

Staelin, D. H., Kerekes, J. P., and F.J. Solman III, Geosynchronous microwave sounder working group, final report, Mass. Inst. of Technol., Lincoln Lab., Lexington, Mass., 1997.

Wilheit, T. T., Jr., A model for the microwave emissivity of the ocean's surface as a function of wind speed, *IEEE Trans. Geosci. Electron., GE-17* (4), 244-249, 1979.

A.J. Gasiewski and M. Klein, NOAA/ETL, R/E/ET1, 325 Broadway, Boulder Co. 80303. (agasiewski@etl.noaa.gov, mklein@etl.noaa.gov.)

(Received August 20, 1999; revised January 3, 2000; accepted January 13, 2000.)